ELSEVIER

Contents lists available at ScienceDirect

Acta Biomaterialia

journal homepage: www.elsevier.com/locate/actbio



Full length article

Modulation of the mechanosensing of mesenchymal stem cells by laser-induced patterning for the acceleration of tissue reconstruction through the Wnt/ β -catenin signaling pathway activation



Jieni Fu^a, Xiangmei Liu^{a,*}, Lei Tan^a, Zhenduo Cui^b, Yanqin Liang^b, Zhaoyang Li^b, Shengli Zhu^b, Yufeng Zheng^c, Kelvin Wai Kwok Yeung^d, Paul K Chu^e, Shuilin Wu^{a,b,**}

- ^a Ministry-of-Education Key Laboratory for the Green Preparation and Application of Functional Materials, Hubei Key Laboratory of Polymer Materials, School of Materials Science & Engineering, Hubei University, Wuhan 430062, China
- b School of Materials Science & Engineering, the Key Laboratory of Advanced Ceramics and Machining Technology by the Ministry of Education of China, Tianjin University, Tianjin 300072, China
- ^c State Key Laboratory for Turbulence and Complex System and Department of Materials Science and Engineering, College of Engineering, Peking University, Beijing 100871, China
- d Department of Orthopaedics & Traumatology, Li KaShing Faculty of Medicine, The University of Hong Kong, Pokfulam, Hong Kong 999077, China
- ^e Department of Physics and Department of Materials Science and Engineering, City University of Hong Kong, Tat Chee Avenue, Kowloon, Hong Kong 999077, China

ARTICLE INFO

Article history:
Received 3 August 2019
Revised 22 October 2019
Accepted 29 October 2019
Available online 1 November 2019

Reywords:
Laser
Mesenchymal stem cells
Signaling pathway
Implants
Mechanosensing
Surface modification

ABSTRACT

Growing evidence suggests that the physical microenvironment can guide cell fate. However, cells sense cues from the adjacent physical microenvironment over a limited distance. In the present study, murine mesenchymal stem cells (MSCs) and murine preosteoblastic cells (MC3T3-E1) behaviors are regulated by the cell-material interface using ordered-micro and disordered-nano patterned structures on Ti implants. The optimal bone formation structure is a stable wave (horizontal direction: ridge, $2.7 \mu m$; grooves, 5.3 µm; and vertical direction: distance, 700 µm) with the appropriate density of nano-branches (6.0 per μ m²). The repeated waves provide cells with directional guidance, and the disordered branches influence cell geometry by providing different spacing and density nanostructure. And micro-nano patterned structure can provide biophysical cues to direct cell phenotype development, including cell size, shape, and orientation, to influence cellular processes including survival, growth, and differentiation. Thus, the overlaid isotropic and anisotropic cues, ordered-micro and disordered-nano patterned structures, could transfer further and alter cell shape and induce nuclear orientation by activating Wnt/ β catenin signaling to promote integrin α 5, integrin β 1, cadherin 2, Runx2, Opn, and Ocn. That canonical Wnt signaling inhibitor dickkopf1 further demonstrates osteogenic differentiation induced by orderedmicro and disordered-nano patterned structures, which is related to Wnt/ β -catenin signaling. Our findings show the role of ordered microstructures and disordered nanostructures in modulating stem cell differentiation with potential medical applications.

E-mail addresses: liuxiangmei1978@163.com (X. Liu), shuilin.wu@gmail.com, shuilinwu@tju.edu.cn (S. Wu).

^{*} Corresponding author.

^{**} Corresponding author at: Ministry-of-Education Key Laboratory for the Green Preparation and Application of Functional Materials, Hubei Key Laboratory of Polymer Materials, School of Materials Science & Engineering, Hubei University, Wuhan 430062, China.

Statement of significance

It remains a challenge to modify poor osteogenic and osteoconductive properties of titanium alloy bases on the inherent poverty of titanium. We demonstrate that ordered microtopography and disordered nano topography pattern structure could lead to osteogenic differentiation *in vitro* and bone regeneration *in vivo*. Furthermore, the pattern structure is created through selective laser melting and alkali heat. And the structure only takes advantage of titanium itself and does not bring in active film, such as hydroxyapatite. On the other hand, we find that cell shape and orientation show angle-orientation tendency due to the polarity, which involves with mechanical signal created *via* patterned structure. Meanwhile, the Wnt/Ca²⁺ signaling pathway is activated.

© 2019 Acta Materialia Inc. Published by Elsevier Ltd. All rights reserved.

1. Introduction

The morphogenesis of biological cells is crucial to most physiological processes [1-4]. It is also essential for osteogenic differentiation and ultimately bone regeneration [5–7]. Cell guidance can be provided by external cues, such as chemical concentrations, substrate rigidity and substrate topography [8-10]. A major challenge of guiding live cells at the bone-implant interface is that they can sense their microenvironment over a limited distance. Relaying chemotactic signals can overcome this limit. However, using chemical cues to relay chemotactic signals requires intricate orchestration and timing of signals [8,11,12]. Surface topography is another method by which to alter cell orientation over large distances [13]. Surface nanotopography on implants, including ridges and grooves [14,15] or aligned collagen fibers [14], could serve to modulate them. However, the nano-patterns structures examined in previous studies have merely offered bidirectional guidance, resulting in a tendency for cells to assume an elongated and round shape, which may induce osteogenic and adipogenic differentiation. Surface nanotopography alone induces different effects on single cells via receptors of cell adhesion [16], and this structure of mature bone is a micro-nano structure [17]. Surface microtopography is another type of surface topography. Ordered microstructures are common cues that influence cell morphology and spreading [18]. However, microtopography can alter entire cell behaviors. Moreover, several researchers have suggested that microscale texture alone may inhibit cell adhesion and cell proliferation [19]. Additionally, ordered-micro structures are often obtained by soft lithography, electron beam lithography, anodic aluminum oxide. and block copolymer lithography [9,20-22]. However, these approaches are more suitable for thin nonmetallic substrates and involve hazardous reagents, such as hydrogen fluoride [21].

It is well known that the extracellular microenvironment comprises nanotopography and microtopography [9,23]. Interestingly, previous works have demonstrated that surface microtopography and nanotopography could alter cell shape and improve osseointegration at the cell-implant interface, which is known as contact guidance [24]. On the other hand, there are four objects including commercially pure titanium and three titanium alloys (Ti-6Al-4V, Ti-6Al-4V Extra Low Interstitial [low components] and Ti-Al-Nb). And pure titanium and Ti-6Al-4V are used in biomaterial. Titanium has great corrosion resistance and good biocompatibility due to oxide layer of nanometer thickness at the surface of titanium. And oxide on the surface of titanium leads to bioinert poverty, which caused poor osteointegration [19,25]. Creating nanotopography and microtopography that is similar to the extracellular structure is an effective way to overcome this disadvantage. However, there is a distinct lack of simple, safe fabrication techniques to create ordered-micro and disordered-nano topography on Ti surfaces to study cell-biomaterial interactions.

Despite a limited role of Ti implants in improving osseointegration, mechanisms altering cell shape through local microen-

vironment have been illustrated [6]. Although several reports have indicated that cells respond to ordered microtopography and disordered nanotopography, several studies indicate that different substrate rigidities lead to various cell behaviors [17,26–28]. Without systematic research constructing the ordered-micro and disordered-nano topographies through Ti itself, it is hard to draw strong conclusions and fundamentally improve the poor osseointegration associated with Ti implants.

In the present study, this challenge is tackled by designing biomaterials with ordered-micro and disordered-nano topography on Ti surfaces. The former structure is created by selective laser melting, and the latter is obtained through alkali-heat treatment. The two steps could create the ultimate structure. These processes are safe and simple, and the components are only Ti, O, and K (with no other osteogenic elements). The ordered microtopography led to cell anisotropy, and the disordered nanotopography led to isotropic effects. We find that the physical cues provided by ordered-micro and disordered-nano topography physically constrain cell shapes, and then spontaneously translate matrix alignment to a mechanical signal through cellular guidance. Thus, cell nuclear shape and orientation are key signals for contact guidance. First, cells use their own integrin $\alpha 5$ and integrin $\beta 1$ to sense and adhere to patterned Ti. Second, the actin in the cells aligns and cell nuclei begin to align. the MSCs and MC3T3-E1 differentiate into osteoblast. The Ti-LA-AT₂ surface can significantly upregulate the expression of Runt-related transcription factor 2 (Runx2, a pivotal transcription factor that can regulate bone formation), Alp (an early marker of the bone matrix remodeling process), osteocalcin (Ocn, a latestage marker gene that has significant function during embryonic osteogenesis and the bone remodeling process), osteopontin (Opn, a typical bone-specific extracellular matrix protein) and β -catenin, thus significantly promoting bone regeneration. The modulation of signaling pathways of osteogenic differentiation is schematically illustrated in Fig. 1. Furthermore, our findings systematically explain the difference in response to the contact environment across differently patterned structures and offer a biophysical enlightenment of the principles of biomaterial design.

2. Materials and methods

2.1. Materials

Two kinds of commercially pure titanium plates (ϕ 14 × 2.5 mm and ϕ 22 × 2 mm) were purchased from Shanghai Baosteel Co. Ltd, China. The former was used for general tests, including materials characterization and cell culture, while the latter was employed for culturing cells for Western blot (WB) and quantitative real-time reverse transcription chain reaction (qRT-PCR) analysis. All laboratory chemical reagents were bought from Aladdin BioChemical (Los Angeles, CA) unless otherwise noted. Tissue culture plastic (12 well plates and 24 well plates) was purchased from Nest. Cell culture media and 0.05% trypsin-EDTA were purchased from

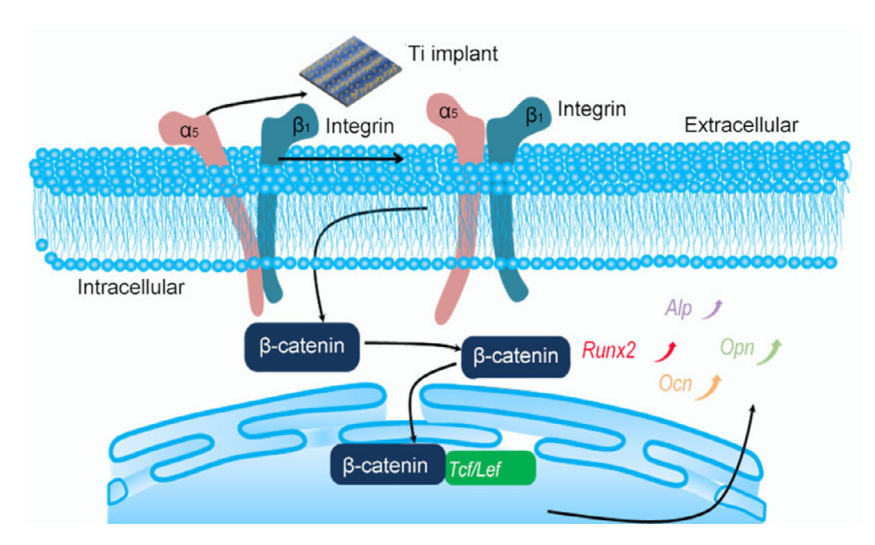


Fig. 1. Schematic illustration of patterned Ti for osteogenic differentiation. (i) Activation of integrin $\alpha_5\beta_1$ heterodimers and regulation of cell morphology. (ii) Stimulation of MSCs and MC3T3-E1 related gene and β -catenin expressions to promote osteogenic differentiation.

HyClone. Fetal bovine serum was obtained from Gibco. The alkaline phosphatase assay kit (AKP Microplate test kit) was purchased from Nanjing JianCheng Bioengineering Institute. BCA Protein Assay kit goat serum was purchased from Solarbio (Beijing, China). 4, 6-diamidino-2-phenylindole (DAPI), FITC conjugated phalloidin (actin), SDS-PAGE gels, and β -actin (rabbit, multiclonal) were purchased from Yeasen (Shanghai, China). Osteocalcin (mouse monoclonal anti-OCN, proteintech), osteopontin (mouse monoclonal anti-OPN, proteintech), and goat antimouse secondary antibodies labeled by TRICT were purchased from Proteintech. The β -Catenin (rabbit, monoclonal) was purchased from Abcam. A Total RNA Kit was purchased from Omega. PrimeScript RT Master Mix and 2 × SYBR Premix Ex Taq II were purchased from TaKaRa. Nitrocellulose membrane was purchased from Millipore. ClarityTM Western ECL Substrate (peroxide solution and luminol/enhancer solution) was purchased from Bio-rad. RIPA lysis buffer, primary antibody dilution, and secondary antibody dilution were obtained from Wuhan Servicebio Technology Co. 5 x blocking buffer and $10 \times$ washing buffer were from ScanLaterTM.

2.2. Synthesis of Ti-At₂, Ti-La (x), and Ti-La-Atx

Ti plates were polished via SiC paper of 240, 400, 800, and 1200 grids, sequentially. After that, acetone, ethanol, and deionized water (ddH₂O) were used for ultrasonic cleaning, respectively. After drying, the Ti plates were immersed in a mixed acid solution (1 HF, 4 HNO₃, and 5 DI (volume) for 2 min to clear the surface oxide layer. These were then cleaned and dried as the control group, which was named Ti. Surface micro-patterning of the Ti plates was performed on a laser instrument (wavelength 1.06 µm, LUMONICS, JHM-1GY-300B). The patterned structure depended on processing parameters and fiber laser and rectangular scanning strategy. The laser current (I) was 70 A, 80 A, and 90 A, respectively. Laser frequency (f) was 20 Hz, the laser spot diameter (D) was $600 \,\mu\text{m}$, scanning velocity (V) was 0.5 mm/s (x-direction), and the translation step in the y-direction was $700 \,\mu\text{m}$. The laser beam scanning strategy was linear scanning in the x-direction, and that was translated in the y-direction. The Ti plates were fixed on to the specimen stage and a laser beam was moved back and forth quickly according to the predetermined program. First, the laser-treated samples were labeled Ti-LA. The Ti-LA obtained with 70 A, 80 A, and 90 A laser current were named Ti-LA (70 A), Ti-LA (80 A), and Ti-LA (90 A), respectively. Second, the Ti-LA (80 A) were treated at 120 °C for 120 min for alkali treatment (AT) with 1 M, 2 M, and 4 M KOH, respectively, and the corresponding samples were designated as Ti-LA-AT1, Ti-LA-AT2, and Ti-LA-AT4. Third, the Ti, treated with 1 M, 2 M, and 4 M KOH, respectively, were named Ti-AT1, Ti-AT2, and Ti-AT4. Fourth, the different samples of Ti-LA (70 A), Ti-LA (80 A), and Ti-LA (90 A) treated with 2 M KOH were named as 70 A-2 M, 80 A-2 M, and 90 A-2 M, respectively. The laser current was bigger, and the energy was higher. All the samples were cleaned and then dried for further use.

2.3. Characterization of Ti-At₂, Ti-La (x), and Ti-La-Atx

Scanning electron microscopy (SEM)/energy dispersive X-ray spectroscopy (EDS) (JSM-6510LV, Japan), and field-emission scanning electron microscopy (FE-SEM)/EDS (Zeiss Sigma 500, Germany) were used to analyze the Ti surface's morphology and composition after platinum was sputtered-coated to improve the electrical conductivity. X-ray diffraction (XRD, Rigaku, Japan) was used to identify the material phase. The metal target was Cu ($\lambda=1.540598\,\text{Å}$). The diffraction angles ranged from 20° to 70°, and the step size was 0.02°. The elemental chemical states were analyzed *via* X-ray photoelectron spectroscopy (XPS, Thermo Fisher Scientific 250Xi, USA). The roughness was determined using an Atomic Force Microscope (AFM, Solver Nano, Bruker, Camarillo, CA). Water contact angles were obtained through a contact angle instrument (OCA 17340, Filderstadt, Germany) at room temperature.

2.4. Electrochemical measurement

Potentiodynamic polarization (PDP) was performed to evaluate the corrosion resistance of the different samples at 37 °C in phosphate-buffered saline (PBS), according to a previous study [29]. A three-electrode system was used in this experiment, including the working electrode (specimens), reference electrode (saturated calomel electrode), and counter electrode (platinum electrode).

2.5. Immersion tests

The *in vitro* degradation of samples was studied by immersion of samples in NaCl solution (0.9%, $37\,^{\circ}$ C) for 21 days. Then the immersed products were further examined by XRD to compare the curves.

2.6. In vitro apatite formation

The protocol was used to obtain 1.5 times the simulated body fluid (1.5 \times SBF). After the laser or alkali treatment, the samples were immersed separately in 1.5 \times SBF at 37 °C for 3 days to grow apatite, and the 1.5 \times SBF was refreshed every two days. The composition of 1.5 \times SBF was from protocol. [30] Table S1 shows the chemical composition of the 1.5 \times SBF.

2.7. Cell culture

The osteoprogenitor cells of MC3T3-E1 and the MSCs were obtained from Tongji Hospital in Wuhan, China. The MC3T3-E1 should be incubated less than 30 generations. For MC3T3-E1, the cell was cultured in growth medium (89% α -MEM, 1% (10,000 IU/mL penicillin and 10,000 g/mL streptomycin), 10% fetal bovine serum), using a standard cultivation environment (37 °C, 5% CO2, humid environment). When the volume of cells had reached 80% of the volume of the total culture bottle, the cells were passaged via 0.05% trypsin-EDTA in a cell culture incubator for 45 s and then centrifuged at 140 g for 4 min (37 °C). The growth medium was renewed every 3 days. For MSCs, the primary growth media include 89% L-DMEM, 1% (100 U/mL penicillin, and 100 mg/ml streptomycin), and 10% fetal bovine serum. The growth medium was renewed every 3 days. Three passage cells were used in the following cell experiments.

For the osteogenic differentiation experiment, the growth medium was transferred into the osteogenic differentiation medium (growth medium, with the addition of 10 mM of β -glycerol phosphate, $10\times 10^{-9}\, M$ dexamethasone, and $50\,\mu g/mL$ of L-ascorbic acid) after incubating for 24–48 h. Finally, tackling the plated cells was essential at different incubation time prior to evaluation.

2.8. Statistical analysis of cell adhesion

First, the cell suspension (500 μ L, 10⁴ cells/mL) was to the various surfaces and incubated for 48 h. Second, the growth medium was discarded and then 4% formaldehyde solution added to fix the cells. Third, the 4% formaldehyde solution was cleaned and FITCconjugated phalloidin (actin) was diluted with PBS at the ratio of 1:200. Fourth, PBS was used to remove excessive dye and then 4', 6-diamidino-2-phenylindole (DAPI) was employed to stain the cell nuclei. Finally, a laser scanning confocal microscope (Nikon A1 Si, Japan), using a 10x objective (CFI Plan Apochromat, Nikon; NA 0.45, W.D. 4.00 mm), was used to take photos. Images of 1024×1024 pixels were taken at a zoom of 1.0. Images were collected and saved at 12-bit resolution for quantitative calculation of the cell nuclei orientation angle. First, the raw imaging data were opened for viewing in a NIS-Elements Viewer. The -Z view was chosen to show the images. Meanwhile, the definition of cell nuclear orientation angle was presented in Fig. 5(a). Image J software was used to quantify the cell nucleus area and the cell nucleus aspect area.

To further identify the cell adhesion, the cells were cultivated for 48 h and then immersed in 2.5% glutaraldehyde solution for 2 h. The next step was to be dehydrated using graded ethanol/ddH $_2$ O ratios (10/90, 30/70, 50/50, 70/30, 90/10, and 100/0, respectively) for 15 min. Then, the cells were placed in an oven at 60 °C overnight to dry. Afterwards, dried samples were splattered with platinum film, and used to obtain images at 10 kV with FE-SEM.

2.9. MTT cytotoxicity test

The viability of cells was assessed *via* a methyl thiazolyl tetrazolium (MTT)-based cytotoxicity assay. 10⁴ cells/well were seeded

on each specimen. The cells were then cultured for 1, 3, and 7 days in a growth medium, which was refreshed every 3 days. At the different incubation time, the growth medium was changed to $0.5 \, \text{mg/mL}$ MTT and the cells were incubated in a cell incubator for 4 h. Next, the MTT solution was discarded and an equal volume of dimethyl sulfoxide (DMSO) added to dissolve formazan. Finally, $100 \, \mu \text{L}$ DMSO of the mixed solution was extracted to measure OD data on a microplate reader at 570 nm. The experiment involved three parallel groups. The detailed reduction of viability compared to the pure Ti was calculated by the following equation:

$$Viab.\% = (100 * OD_{570e})/OD_{570b} * 100\%$$
 (1)

where OD_{570e} represents the mean optical density of the treated sample and OD_{570b} is the mean value of optical density of pure Ti.

2.10. Total intracellular protein and ALP assays

The cells were cultured in a 24-well plate, with 10⁴ cells in each hole. When the cells had been incubated in growth medium for 24–48 h, the growth medium was changed to an osteogenic differentiation medium and the cells incubated for 3, 7, and 14 days, after which they were lysed with 0.1% Triton X-100 for 1 h at 37 °C. Cell lysis solutions were further used to measure alkaline phosphatase content with an ALP assay kit and total protein with a BCA protein assay kit, using bovine serum albumin (BSA) as a standard. The OD value from the former were measured on a microplate reader at 520 nm, and the OD value from the latter on a microplate reader at 562 nm. The ALP activity was normalized to the protein amount. The experiment involved three parallel groups.

2.11. qRT-PCR assay

The 10^4 cells/mL were seeded into every well in a 12-well plate. After the cells had been incubated in growth medium for 24–48 h, the growth medium was changed to an osteogenic differentiation medium. After culturing in the osteogenic differentiation media for 14 days, the cells were extracted from the total RNA using a Total RNA Kit. And then, cDNA was obtained *via* reverse-transcription from 500 ng of the extracted cellular RNA using PrimeScript RT Master Mix. Finally, qRT-PCR was done through $2 \times SYBR$ Premix Ex Taq II with the CFX ConnectTM Real-Time System (first, 10 min hot start at $95\,^{\circ}$ C; second, 45 cycles of $15\,s$ at $95\,^{\circ}$ C; third, $10\,s$ at $60\,^{\circ}$ C, and $30\,s$ at $72\,^{\circ}$ C.). The expression levels of the mRNAs were standardized through the expression level of β -actin and Gapdh. The primer sequences of the MC3T3-E1 cells were shown in Table S2; Table S3 showed the primer sequences of the MSCs.

2.12. Immunofluorescence staining

10⁴ cells were added into every well in 24-well plate. The growth medium was changed to an osteogenic differentiation medium after the cells had been cultured for 24-48 h in growth medium. Different cells were cultured for different times. The MC3T3-E1 (10 d) and MSCs (3 d, 7 d, and 14 d) in the five different groups were immersed in a 4% formaldehyde solution for 20 min after cultivation in osteogenic medium for several days. In the next step, PBS was used to eliminate excessive formaldehyde. And then, the cells were permeated through 0.1% Triton X-100, after which the cells were cleaned with PBS and cells immerged into 10% goat serum solution for 1 h at 37 °C. Next, primary antibodies (mouse monoclonal anti-OCN and mouse monoclonal anti-OPN) were added at 4 °C for 12 h. The mouse monoclonal anti-OCN and mouse monoclonal anti-OPN were diluted to 1:200 using PBS. Furthmore, the cells were then cleaned through PBS and goat anti-mouse secondary antibodies labeled by TRICT (1:100 dilutions in PBS) added at 37 °C for 1 h. Finally, the excessive second antibody was removed with PBS, and the actin cytoskeleton and cell nuclei were further stained with actin and DAPI. In the last step, images of immunofluorescence staining were obtained with an Inverted Fluorescence Microscope (IFM, Olympus, IX73). Image J software was used to quantify the ratio of the OPN/OCN area to the total cell area. In addition, after MSCs had been cultured on the surface of Ti and Ti-LA-AT₂ for 7 days, the cells were stained with cadherin 2 (rabbit polyclonal anti-cadherin 2; 1:200 in PBS), and the process followed as in the previous step.

2.13. Mineralization assay

10⁴ cells/mL cell suspension was added into different samples in a 12-well plate. After culturing 24-48 h in their own growth medium, the medium was changed to an osteogenic differentiation medium. MC3T3-E1 and MSCs were cultured for an appropriate time in their own osteogenic differentiation medium. As for MC3T3-E1, the appropriate culturing time was 10 d, whereas for MSCs, the appropriate culturing time points are 3 d, 7 d and 21 d. First, the osteogenic medium was discarded and cleaned with PBS three times. Second, 4% paraformaldehyde was used to fix the cells for 15 min at room temperature, after which it was discarded and the cells washed with PBS three times. Finally, these were immerged into Alizarin Red Staining (pH 7.4) solution for 10 min. A digital camera took photos of the dried samples. For further quantitative analysis, 10% cetylpyridinium chloride (10% w/v 10 mM sodium phosphate (pH 7.0)) was added for 1 h at room temperature. The results were measured by microplate reader at 562 nm.

2.14. Western blot assay

The 30,000 MSCs were added into a 12-well plate. After culturing in growth medium, the growth medium was switched to an osteogenic differentiation medium and the cells cultured in their own osteogenic medium for 14 days. First, they were harvested and lysed with RIPA lysis buffer on ice for 10 min. Second, the solution was collected in 1.5 mL Eppendorf tubes. Third, Eppendorf tubes were centrifuged at 9710 g for 10 min at 4 °C. The supernatants were then harvested. Fourth, a BCA kit was used to obtain the protein concentration. Fifth, the protein samples were denatured by boiling for 10 min and loaded 20 µg on to SDS-PAGE gels. Sixth, transferring the proteins to the protein nitrocellulose membrane, the membranes were blocked in 1 \times blocking buffer at 37 °C for 1 h. Then, the membranes were placed at 4 °C for 12 h with primary antibodies, with β -Catenin at 1:4000 dilution and β -actin at 1:2000 dilution. And then, the membranes were then cleaned with the 1 × washing buffer three times. Next, the goat anti-rabbit secondary antibody, 1:1000 dilution, was added to incubate the membranes for 1 h at 37 °C. Finally, the cultured membranes were immerged into the buffer to rinse off the second antibody, and the results were assessed by chemiluminescence (ECL system, Amersham Biosciences, Piscataway, NJ). The quantitative analysis was performed in Image-pro Plus software.

2.15. DKK1 treatment

The 10⁵ MSCs were added into the surface of different samples in a 12-well plate and cultured for 24 h in growth medium, which was then switched to osteogenic differentiation medium supplemented with Wnt inhibitor recombinant human dickkopf related protein-1 (HEK293-expressed) (DKK1; 100 ng/mL; MedChem-Express; Monmouth Junction, NJ, USA). Mineralization assay and qRT-PCR assay were performed after culturing for 7 d. The MSCs were seeded on the surface of different samples without DKK1 as a control group.

2.16. In vivo rat tibia implantation model

400 g-450 g male Sprague-Dawley (SD) rats were purchased from the Wuhan Centers for Disease Prevention & Control to evaluate the in vivo bone regeneration ability of the patterned Ti implants. All animal experiments were performed by the animal research committee of Tongji Medical College, Huazhong University of Science and Technology (Wuhan, China). There were 15 male rats, and the leg of every rat was examined (n=6 per group). The bilateral tibias of the rats were all implanted Ti rods. The five groups were: (1) Ti, (2) Ti-AT₂, (3) Ti-LA-AT₁, (4) Ti-LA-AT₂, and (5) Ti-LA-AT₄. First, the rats were placed under general anesthesia via intraperitoneal injection of pentobarbital (30 mg/kg, 1% w/w), and then the surgical site was sterilized with iodophor disinfectant. Afterward, a hand drill was used to drill a hole with a diameter of 2.0 mm, followed by application of physiological saline to clean the bone cavities. Finally, the implants were placed into the prepared holes. The tibia would be obtained after 4 weeks. The rats had abundant food and water during the tests.

2.17. X-ray and bone micro-CT analysis

X-ray pictures were obtained from the rats after 4 weeks to confirm the implantation of the Ti implant. The Micro-CT system (USDA Grand Forks Human Nutrition Research Center, Grand Forks, ND) was used to perform quantitative analysis of the gross bone morphology and microarchitecture.

2.18. Histopathological and cross-sectional evaluation

The samples were processed by Safranin-O and Fast Green staining, Van Gieson's picro fuchsin staining and immunohistochemical staining by iNOS and TGF β . The first was used to evaluate the osteogenic differentiation or chondrogenic differentiation on implants. Green represented osteogenesis, and red or orange stood for cartilage. The osteogenesis ratio was defined as the percentage of osteogenesis within the whole tissue region (a region extending $100 \, \mu \text{m}$ from the implant surface). The second was used to analyze the mineralized bone tissue (red) around the implantbone interface. The bone area ratio was the percentage of mineralized bone within the whole tissue region (a region extending $250\,\mu m$ from the implant surface). The bone-to-implant ratio was the percentage of adhered bone on the bone-to-implant interface (a region extending $250 \, \mu \text{m}$ from the implant surface). The third was used to analyze the inflammation around the implant. The images were collected by a Pannoramic SCAN digital slide scanner (3DHISTECH Ltd, Budapest, Hungary). Quantitative analysis was performed using Image J software. For cross sectional analysis, the sections were analyzed using FE-SEM equipped with

2.19. Statistical analysis

All the experimental data were analyzed via one-way ANOVA or two-way ANOVA using GraphPad Prism software. The number of samples was equal to or more than 3. *p < 0.05 was considered statistically significant. All data from $in\ vitro$ and $in\ vivo$ were presented with mean \pm standard deviation (SD).

3. Results

3.1. Characteristics of Ti-AT₂, Ti-LA (x), and Ti-LA-ATx

Fig. 2(a) shows the fabrication process of Ti-LA (Ti was treated with an 80 A laser current), Ti-LA-AT_x (Ti-LA was treated at

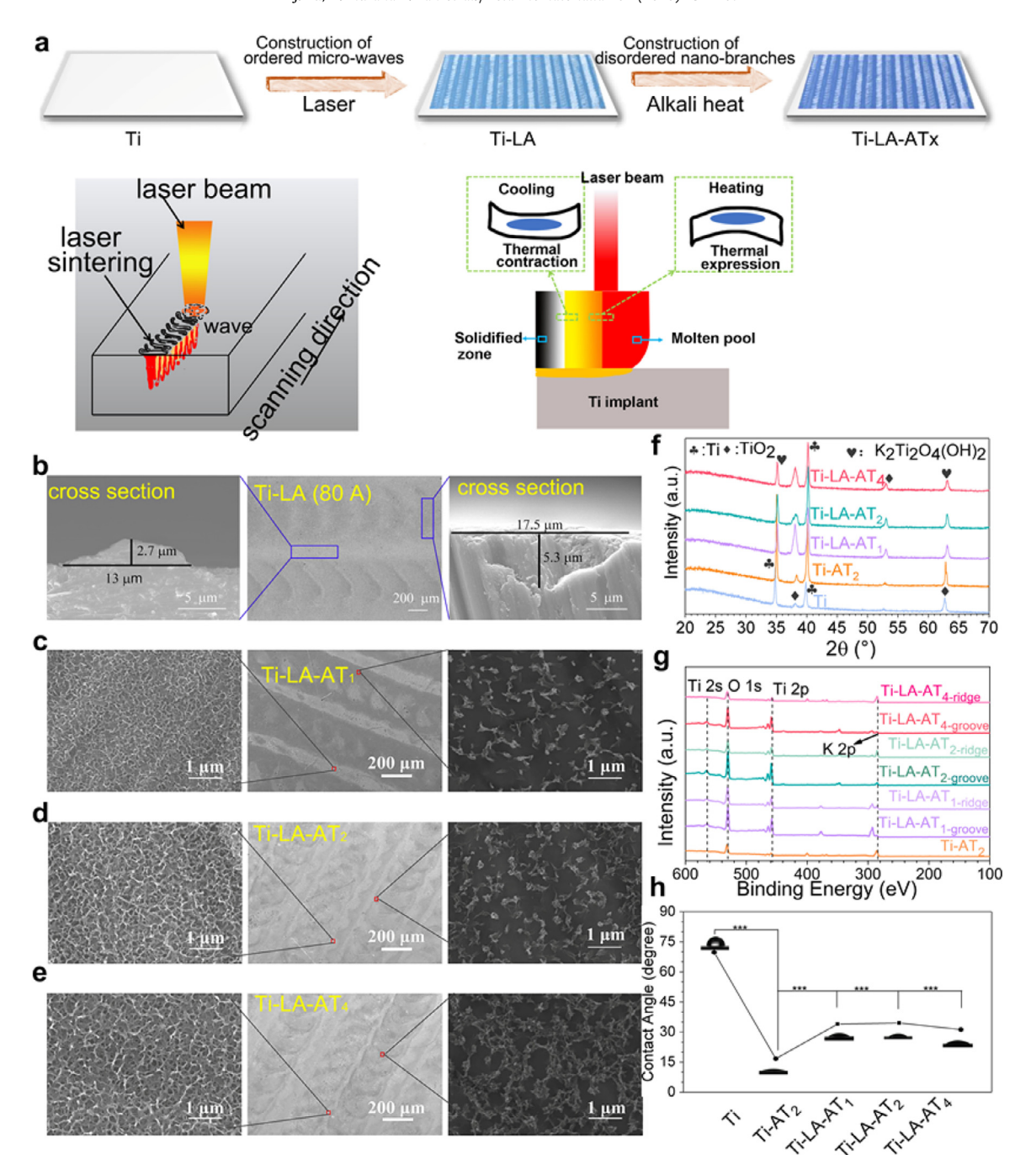


Fig. 2. Illustration of reaction process and characterization of different samples. (a) Schematic illustration of the fabrication process of Ti-LA-AT $_{\chi}$ and the principle of wave formation and selective laser melting. (b) Surface morphology of the Ti-LA. On the left is a vertical cross-section of Ti-LA; on the right is a horizontal cross-section of Ti-LA. (c-e) Surface morphology of the different samples (Ti-LA-AT $_{\chi}$, Ti-LA-AT $_{\chi}$, and Ti-LA-AT $_{\chi}$). The overall appearance is shown in the center. The morphology of the ridges is shown on the left and that of the wave-like structure on the right. (f) XRD patterns of the various Ti surfaces. (g) XPS survey spectra of the different samples in different areas. (h) Contract angles of five samples.

120 °C for 120 min in a hydrothermal synthesis reactor with x M KOH, x=1, 2, and 4), and the mechanical actions of a selective melting laser. The pulse laser radiates on the surface of the Ti sheet and causes local overheating, owing to the transiently high temperature, leading to obvious temperature gradients and varied surface tension as well as Marangoni convection effects. Formation of the convective streams increase the magnitude of the thermocapillary force, and the radially inward flows lead to the formation of a relatively coarsened wave, which in turn induces the formation of grooves and ridges. The height of the grooves and ridges is related to the energy of the selective laser melting. [31,32] Fig. S1a and b shows the surface mor-

phology of Ti-LA. A wave-like micropatterned topography forms on the Ti plate. Line-by-line laser exposure forms a parallel line structure. The laser spot diameter is $600\,\mu\text{m}$, which is smaller than the *y*-direction translation distance of $700\,\mu\text{m}$. Therefore, the melted areas do not overlap. The distance between two waves is approximately $300\,\mu\text{m}$ during the *y*-axis and $200\,\mu\text{m}$ during the *x*-axis. The width of the wave is approximately $550\,\mu\text{m}$ owing to weak energy at the edge of the laser pulse. The height of the ridge is approximately $2.7\pm1.3304\,\mu\text{m}$, and the depth of the groove is approximately $5.3\pm0.94113\,\mu\text{m}$ (Fig. 2(b)). As shown in Fig. 2(c)–(e), the patterned micro-waves also possess a nanoscale surface topography. The surface topography varies between

grooves and ridges (Fig. 2(c)–(e), left column and right column). After the alkali and heat treatments, the original wave-like structure between two adjacent ridges is retained. Meanwhile, Ti-LA-AT $_1$, Ti-LA-AT $_2$, and Ti-LA-AT $_4$ obtain new surface topographies compared to Ti-LA (Fig. S2(a) and (b)). The average densities of the nanobranch-like features on Ti-LA-AT $_1$, Ti-LA-AT $_2$, and Ti-LA-AT $_4$ are 3.75 ± 2.55852 , 6.03 ± 2.94596 , and 9.24 ± 2.94774 per μm^2 , respectively.

As shown in Fig. 2(f), there are several crystalline phases. For Ti, the characteristic peaks at 35°, 39.8°, and 53° correspond to the lattice planes of (100), (002), and (102), respectively [33,34]. The peaks of TiO₂ observed at 38° and 63° correspond to the lattice planes of (020) and (002), respectively. After the surface treatment, new peaks emerge. The peaks at 35° and 64° indicate the presence of K₂Ti₂O₄(OH)₂ [35], resulting from the reaction between Ti and KOH. For Ti-LA-AT₁, Ti-LA-AT₂, and Ti-LA-AT₄, there are several differences compared with Ti and Ti-AT₂. The marked peaks from TiO2 at 40° and 53° are enhanced, owing to the selective laser melting. The peaks of Ti-LA-AT₁, Ti-LA-AT₂, and Ti-LA-AT₄ are larger than those of Ti and Ti-AT2. The relative intensity of TiO2 decreases with increasing concentrations of KOH, thanks to the positive relationship between the corrosion ability and the concentration of KOH. The larger the KOH concentration, the smaller the TiO_2 content. The peak at 35 °C decreases compared to $Ti-AT_2$, which is the result of the laser treatment.

The X-ray photoelectron spectroscopy (XPS) survey spectra demonstrate the existence of Ti, C, O, and K in the laser-treated samples (Fig. 2(g)). C is a contaminant and Ti, O, [36] and K originate from the Ti substrate. Ti-LA- $AT_{1-ridge}$ stands for the ridge areas in Ti-LA-AT₁, and Ti-LA-AT_{2-ridge} and Ti-LA-AT_{4-ridge} have similar meanings. Ti-LA-AT $_{1\text{-groove}}$ represents the area of the groove structure in the Ti-LA-AT₁, and Ti-LA-AT_{2-groove} and Ti-LA-AT_{4-grove} have similar meanings. The K 2p signals (\sim 292 eV and \sim 295 eV), Ti 2p signals (approximately 457.8/463.4 eV and 458.41 eV/464.22 eV), and O 1s (approximately 531.5 eV and 532.5 eV) are observed from the survey XPS spectra of all samples. [36] Ti-AT₂ shows Ti, O, and K; compared to Ti-AT₂, the Ti-LA-AT_{1-ridge} and Ti-LA-AT_{1-groove} have more intense peaks of C and O but less of K. This is related to the selective laser melting, which brings oxides to the surface of the samples. When the concentration of KOH is small, as in the case of Ti-LA-AT $_{1-ridge}$ and Ti-LA-AT $_{1-groove}$, the Ti-LA-AT $_{1-groove}$ has a larger level of O, rendering these areas harder to corrode during alkali treatment. Ti-LA-AT_{1-ridge}, Ti-LA-AT_{1-groove}, Ti-LA-AT_{2-ridge}, Ti-LA-AT_{2-groove}, Ti-LA-AT_{4-ridge}, and Ti-LA-AT_{4-groove} show similar phenomena. When the concentration of KOH is larger, the effects of the alkali treatment is more pronounced and a small amount of C disappears from the surface. To obtain more information about Ti from the ridge and groove areas, the XPS high-resolution spectra of Ti 2p from Ti-AT₂, Ti-LA-AT_{2-ridge} and Ti-LA-AT_{2-groove} are acquired (Fig. S3a-c). Ti-LA-AT₁, Ti-LA-AT₂, and Ti-LA-AT₄ show similar results concerning the ridge and groove structures, owing to the similar treatment procedure. For Ti-AT2 and Ti-LA-AT_{2-ridge}, the Ti 2p doublets appear at approximately 458.41 eV and $464.22 \,\mathrm{eV}$ with a skewing $5.9 \,\mathrm{eV}$, corresponding to the Ti^{4+} . For the Ti-LA-AT2-groove, the Ti 2p doublets at 458.41 eV/464.22 eV and $457.8/463.4\,\text{eV}$ are related to Ti^{4+} and Ti^{3+} . [37] The XPS highresolution spectra of O 1s from Ti-AT2, Ti-LA-AT2-ridge and Ti-LA- $AT_{2-groove}$ (Fig. S4a-c) show O-Ti⁴⁺ (530.28 eV), O-O (531.91 eV), H-O (531.52 eV), and O-H (532.3 eV) for Ti-AT₂ and Ti-LA-AT_{2-ridge}. However, there is only one peak at 532.95 eV assigned to O-Ti³⁺ for Ti-LA-AT_{2-groove} [38]. These results are in line with the highresolution spectra of Ti 2p.

The surface hydrophilia has substantial effects on the protein adsorption, which plays a crucial role in cell proliferation and differentiation [39]. To evaluate the effects of the hierarchical structures on hydrophobicity, the static contact angles (CAs) are mea-

sured. As shown in Fig. 2(h), the CA on the untreated Ti is 70°. The CA of Ti-AT₂ shows only the smallest value of 18° The CAs on Ti-LA-AT₁, Ti-LA-AT₂, and Ti-LA-AT₄ are 33°, 32°, and 30°, respectively. Furthermore, the potentiodynamic polarization behavior of different samples in PBS is used to study whether laser- and alkali-heat treatments influence the corrosion of Ti substrates. As shown in Fig. S5a, the Nyquist plots of Ti, Ti-AT₂, Ti-LA-AT₁, Ti-LA-AT₂, and Ti-LA-AT₄ indicate that different samples have a similar cathodic polarization branch, which suggest that the corrosion resistance of Ti-AT₂, Ti-LA-AT₁, Ti-LA-AT₂, and Ti-LA-AT₄ is similar to that of Ti. After 15 days' immerging in NaCl solution, no peak occurred other than that of NaCl (Fig. S5b).

3.2. In vitro evaluation

The alkali-heat treatment produces -OH on the Ti samples superficially, which favors the formation of HA, [40] and the micronano hierarchy structure bodes well for biomineralization [41]. SBF is a broadly accepted *in vitro* method of assessing potential bone regeneration *in vivo*, *via* their apatite-forming ability [42]. And $1.5 \times SBF$ is widely used for growing hydroxyapatite at 37 °C. [30] As shown in Fig. S6a and S6d, a myriad of small precipitates nucleated and grew on the exposed surface of Ti, Ti-AT₂, Ti-LA-AT₁, Ti-LA-AT₂, and Ti-LA-AT₄. The high-magnification images show sphere-like precipitates (Fig. S6e), and the picture of EDS shows the existence of Ca and P (Figs. S6f and S6g). The Ca/P proportion is 1.76, which is similar to hydroxyapatite. The results show that Ti-LA-AT_x has the ability to make co-precipitation of calcium and phosphate ions to form hydroxyapatite, which is the foundation of surface biomineralization [30].

The influence of different laser currents on the depth of micro-groove and the height of micro-ridge is studied via SEM (Fig. 3(a)) and AFM (Figs. 3(b) and S7a-c) to obtain quantitative information and qualitative information on Ti, respectively. In the SEM cross-section image, when Ti is treated with a 70 A laser pulse, the height of the ridge is approximately $1.57 \,\mu\text{m}$, and the depth of the groove is approximately $3.61 \,\mu\text{m}$. After Ti treatment with a 90 A laser, the height of the ridge, as seen in SEM images, is approximately $4.23 \mu m$, and the depth of the groove is approximately 7.43 µm. Additionally, AFM was conducted to support the data in Figs. 3(b) and S7a-c. The height of Ti-LA (70 A), Ti-LA (80 A), and Ti-LA (90 A) increases with increasing laser current. Furthermore, the shape of the MSCs is found via FE-SEM (Figs. 3(c) and (d), and 4) to obtain qualitative information on different micro-topography and nano-topography surfaces.

As shown in Figs. S8a-8c and 3(c), on ordered micro-waves, the MSCs on Ti-LA (90 A) have an arbitrary direction. By contrast, cells alignment on Ti-LA (70 A) are mainly observed at 47.79 $^{\circ}$ \pm 7.88 $^{\circ}$. Furthermore, cells alignment on Ti-LA (80 A) are mainly observed at $32.56^{\circ} \pm 21.62^{\circ}$. Meanwhile, a spreading area of cells on Ti-LA (90 A) represents about 3 times greater than on Ti-LA (70 A) and Ti-LA (80 A) (Fig. S8d). The influence of nanotopography alone on cells are studied further. The density of disordered nano-branches is enlarged with an increasing concentration of KOH. Similarly, the density of nano-branches is growing on Ti-AT₁, Ti-AT₂, and Ti-AT₄. The cells have larger areas and a smaller cell aspect ratio, which can lead to adipogenic differentiation (Figs. 3(d) and S8e). [5,7,43] In addition, as reported in a previous study, cells spread well and exhibit a typical squamous shape on nano-scale topography, and the spreading area is greater than on sub-microns and microns. Contact guidance alters cell behavior by cell-to-sense micro topography to present different orientations and shapes [44,45].

Furthermore, to survey the interactions between cells and micro-nano topography, the Ti surface is functionalized by ordered micro grooves and ridges and disordered nanobranches. As shown

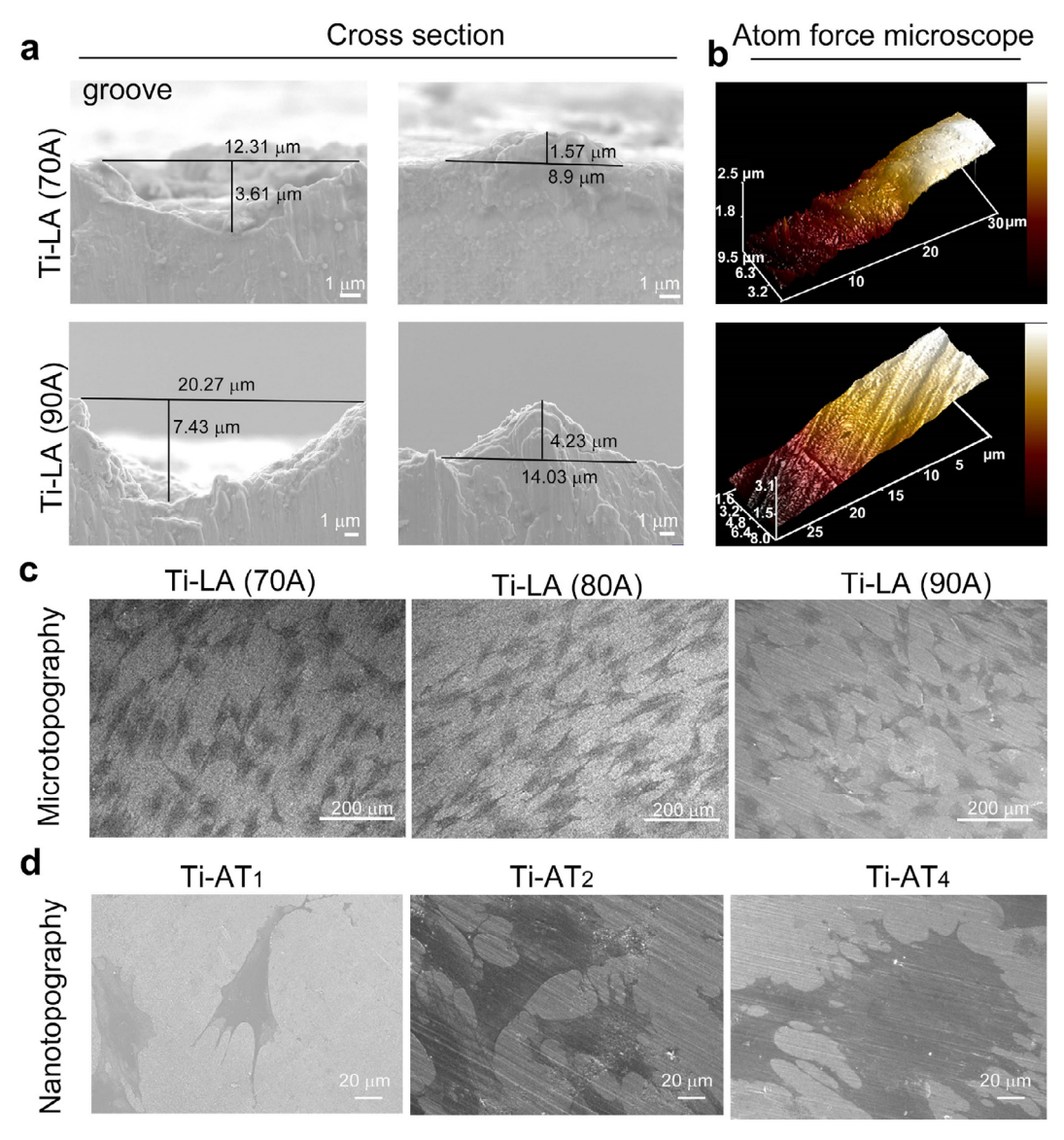


Fig. 3. Illustration of micro/nanotopography's influence on the cell and characterization of different samples. (a) SEM images of cross-section of Ti-LA (70 A) and Ti-LA (90 A). (b) AFM images of Ti-LA (70 A) and Ti-LA (90 A). (c-d) The shape of MSCs on different samples via SEM.

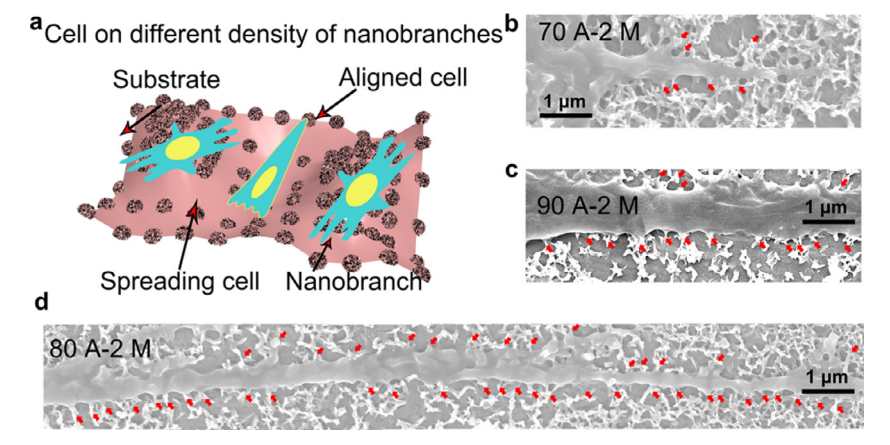
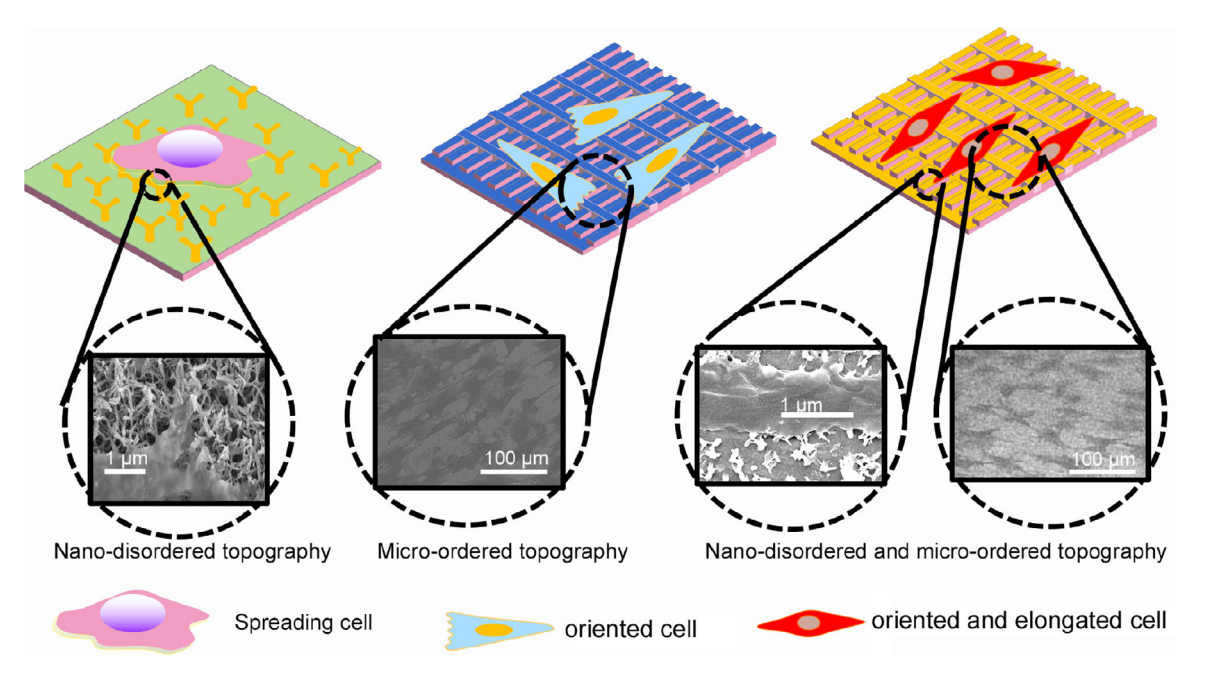


Fig. 4. (a) Schematic illustration of micro/nanotopography's influence on the cell and the cell protrusion of different samples *via* SEM. The interface between cell and materials. Cell protrusion on different samples *via* SEM: (b) Ti-LA (70 A)-AT₂; (c) Ti-LA (90 A)-AT₂; (d) Ti-LA (80 A)-AT₂.



Scheme 1. Schematic illustration of ordered-micro and disordered-nano patterned Ti for cell behaviors.

in Fig. 4(a), cells protrude and sense the branch across a limited distance. In other words, the cues that can modulate cells are local micro/nano topography. When the density and spacing of branches is smaller, the geometry of the cells is rounder [43]. The height of the grooves and ridges is related to the cell orientation. The local micro-nano topography structures translate cues across a certain distance, which leads to cells moving unidirectionally and in an elongated shape. In Figs. 4(b)–(d) and S8f, the red arrows denote the cell–material interface. The more nano-branches, the more the cell protrudes. As shown in Scheme 1, ordered micro topography benefits cell orientation, and nano-disordered topography leads to cell spreading. After selective laser melting and alkaline-heat treatment, the density and spacing of the nanostructure alter, and the cell orientation changes.

MSCs and MC3T3-E1 attach and spread well on different samples (Figs. 5(a) and S9a). However, the cells show the relative orientation on Ti-LA-AT₂ compared with others. In fact, cellular fluorescence is performed in a dark environment and the originally positioned angles of different samples are random. This is the main reason for different dominant angles of different substrates. And, the main angle range is considered as the research object. Compared with Ti and Ti-AT2, the cells can form mature filopodia on Ti-LA-AT₁, Ti-LA-AT₂, and Ti-LA-AT₄ (Fig. S9b). Cellular filopodia on Ti, without nanotopography, tend to be smallest and shortest pseudopodia. In comparison, cells on Ti-AT₂ have more but shorter pseudopodia compared with Ti-LA-AT₁, Ti-LA-AT₂, and Ti-LA-AT₄. Ti-AT₂ has porous nanotopography, which provides more anchors to cells. And Ti-LA-AT₁, Ti-LA-AT₂, and Ti-LA-AT₄ have the same microtopography but different nanotopography. The concentration of KOH is higher, and the density of branches is larger. Compared with Ti and Ti-AT₂, Ti-LA-AT₁, Ti-LA-AT₂, and Ti-LA-AT₄ have additional microtopography. The added microtopography leads to more, longer filopodia. Quantitative analysis of the cellular nucleus orientation angle is performed to understand the relationship between the micro-nanotopography cues and MSCs and MC3T3-E1 behaviors (Figs. 5(a) and S9c-d). Fig. 5(b) shows the definition of aspect ratio and orientation angle. The cell shows the preferred orientation angle in Ti, Ti-LA-AT $_1$, Ti-LA-AT $_2$, and Ti-LA-AT $_4$, owing to the microtopography on the Ti itself. In comparison, there is no significant difference in orientation angle in Ti-AT₂, which indicates the isotropy of nuclei. Ti-LA-AT₂ shows the best performance. Furthermore, the effects of patterned structures on cell nuclear spreading area, aspect ratio, and cell number at different angles are shown in Figs. 5(c)–(d) and S9(e)–(f). The relationship between cell nuclear spreading area and aspect ratio showed a negative correlation on different sample surfaces. The MTT assay was performed to investigate cell cytotoxic activity. As shown in Figs. 5(e) and 59, the Ti-LA-AT₁, Ti-LA-AT₂, and Ti-LA-AT₄ groups showed greater MSC and MC3T3-E1 viability than both Ti and Ti-AT₂ at days 1, 3, and 7. As shown in Fig. 510, laser and hydrothermal treatment have no cytotoxicity effect on MSCs compared with Ti.

The alkaline phosphatase (ALP) serves as an index by which to estimate the early differentiation activity of osteoblasts frequently. [46] Figs. 6(a) and S11 show the ALP activities of Ti, Ti-AT₂, Ti-LA-AT₁, Ti-LA-AT₂, and Ti-LA-AT₄ incubated with MSCs and MC3T3-E1 after 3, 7, and 14 days. The ALP activities of Ti-LA-AT₁ and Ti-LA-AT₄ increase over time. However, Ti-LA-AT₄ shows a bad performance, in part because this structure is favorable for cell proliferation. When the cell density is relatively high, the density becomes harmful to cell osteogenic differentiation. In general, patterned Ti is favorable for MSC osteogenic differentiation. The Ti-LA-AT₂ shows excellent osteogenic differentiation after culturing for 14 days.

To further discuss the osteogenic activity on varied patterned surfaces, a cellular mineralization array is performed on the 10th day using optimal cellular mineralization assays for MC3T3-E1 and on days 3, 7, and 21 for MSCs. Alizarin Red Staining is carried out to assess extracellular microenvironment (ECM) mineralization activity. Mineralized nodules are usually employed to estimate the bone integration of MSC cells and MC3T3-E1 cells. The Ti-LA-AT2 shows the highest values of ECM mineralization (Figs. 6(b), S12–S14). qRT-PCR is further performed to investigate the bone integration gene expression levels. Osteogenic gene expression, including *Runx2*, *Alp*, *Ocn*, and *Opn*, is further evaluated to investigate osteogenic differentiation between MSCs and MC3T3-E1 (Figs. S14, 6(c) and (d)). Ti-LA-AT2 has the best performance in three genes after 3 days, 7 days and 14 days. The expression levels of *Runx2* in MSCs

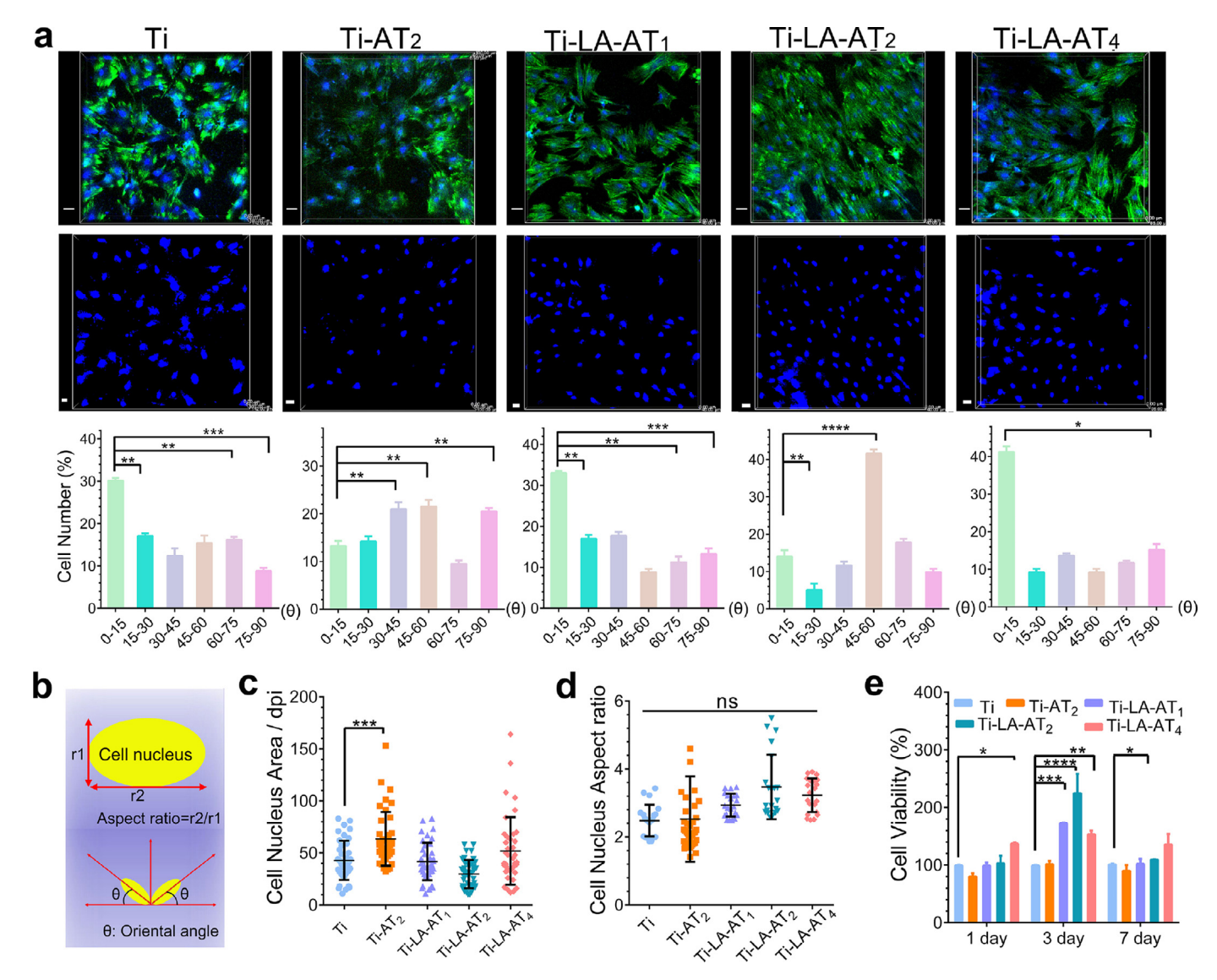


Fig. 5. Different samples (Ti, Ti-AT₂, Ti-LA-AT₁, Ti-LA-AT₂, and Ti-LA-AT₄) can regulate cell nuclei geometric for MSCs. (a) Fluorescence microscopy images of MSCs after 48 h in culture on various samples. The green color represents F-actin and the blue color represents cell nuclei and the orientation angle for different samples. The scale bar is $100\,\mu\text{m}$. (b) The definition of aspect ratio for cells' nucleus and orientation angle. (c) Cell nucleus spreading area in different samples. Mean values and standard deviations from 50 randomly chosen cells. (d) Cell nucleus aspect ratio of various samples. (e) MSCs viability on different samples. The columns in each group are Ti, Ti-LA-AT₁, Ti-LA-AT₂ and Ti-LA-AT₄ in order. Mean values and standard deviations from 50 randomly chosen cells. (a, c, d, e) Data are presented as mean \pm standard deviation (SD); *p < 0.05, **p < 0.01, ***p < 0.001; (a, c, d) One-way analysis of variance (ANOVA) with Dunnett's multiple comparisons test. (e) Two-way ANOVA with Tukey's multiple comparisons test. (For interpretation of the references to color in this figure legend, the reader is referred to the web version of this article.)

incubated with Ti-AT₂, Ti-LA-AT₁, Ti-LA-AT₂, and Ti-LA-AT₄ are upregulated by 1.97, 1.58, 3.43, and 2.38 times and 1.08, 1.29, 2.12, and 0.93 times, respectively, compared to Ti. The expression levels of *Ocn* in MSCs cultured on Ti-AT₂, Ti-LA-AT₁, Ti-LA-AT₂, and Ti-LA-AT₄ are upregulated by almost 1.55, 2.56, 2.9, and 2.37 times and 1.14, 1.20, 1.83, and 1.31 times, respectively, compared to Ti. The expression levels of *Opn* in MSCs cultured on Ti-AT₂, Ti-LA-AT₁, Ti-LA-AT₂, and Ti-LA-AT₄ are upregulated by 0.51, 0.77, 1.63, and 0.52 times and 1.42, 0.97, 2.24, and 1.12 times, respectively, compared to Ti (Fig. 6(c)). Meanwhile, as for MC3T3-E1 at 7 days, Ti-LA-AT₂ has the best performance in three genes after 7 days of culture. In MC3T3-E1 at 14 days, *Runx2* is 0.88, 1.14, 1.97, and 0.62 times greater than Ti; *Alp* is 2.02, 1.19, 4.59, and 2.61 times greater than Ti; and *Ocn* is 1.27, 1.09, 1.91, and 0.45 times greater than Ti (Fig. 6(d)).

Wnt/ β -catenin signaling is a vital pathway that regulates osteogenesis [47]. As shown in Fig. 6(e) and (f), the β -catenin expression of MSCs on Ti-LA-AT₁, Ti-LA-AT₂, and Ti-LA-AT₄ is upregulated, indicating that the ordered-micro and disordered-nano

structures can activate Wnt/ β -catenin signaling. These results indicate that there is a positive correlation between the patterned surface and osteoblast differentiation, consistent with the ALP activity, and that Ti-LA-AT₂ has excellent performance.

To further identify whether Wnt/β -catenin signaling takes part in osteogenic differentiation of MSCs on structure loaded overlaid isotropic and anisotropic cues, integrin $\alpha 5$, integrin $\beta 1$, and cadherin 2 are examined and further DKK1 (Wnt/β -catenin inhibitor) is used to treat MSCs cultured on Ti-LA-AT₂. As shown in Fig. 7(a), the relative mRNA expression of integrin $\alpha 5$, integrin $\beta 1$ and cadherin 2 upregulate after culturing for 7 days, as compared to Ti at 7 days. Meanwhile, the expression of integrin $\alpha 5$, integrin $\beta 1$, and cadherin 2 decrease at day 7 after being treated by DKK1, as compared to Ti-LA-AT₂ (Fig. 7(b)). Alizarin Red Staining further demonstrated that DKK1 inhabits the osteogenic differentiation of MSCs at Ti-LA-AT₂ (Fig. 7(c)). As shown in Fig. S15, the expression of cadherin 2 of Ti-LA-AT₂ is higher than that of Ti.

As shown in Figs. 8(a)-(b) and S16(a)-(d), immunofluorescence staining for MSCs (3, 7, and 14 days) and MC3T3-E1(14 days) is

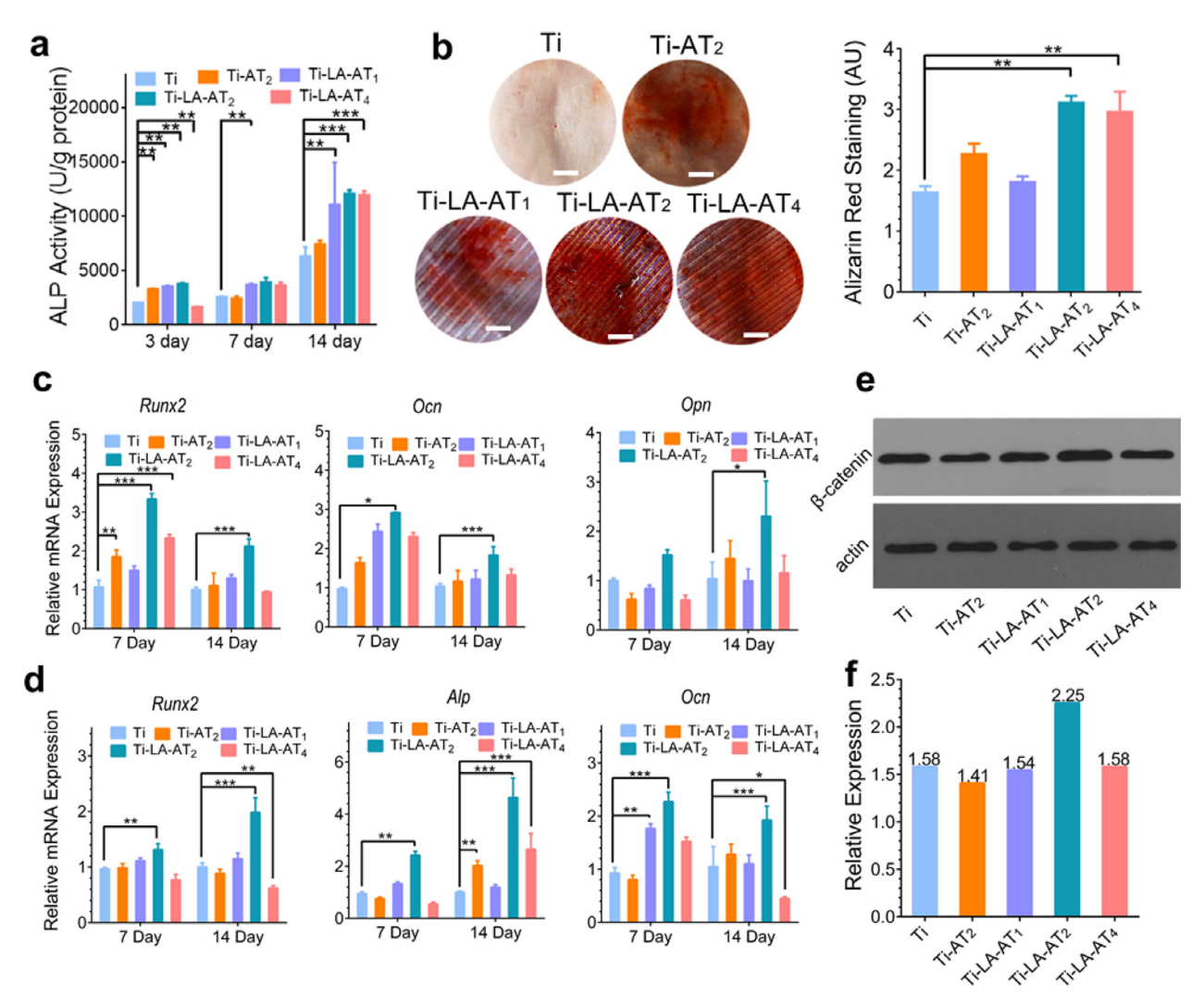


Fig. 6. Different samples (Ti, Ti-AT₂, Ti-LA-AT₁, Ti-LA-AT₂, and Ti-LA-AT₄) can influence the ability for osteogenic differentiation. (a) ALP activity of MSCs after culturing for 3, 7, and 14 days in the osteogenic differentiation medium normalized to total protein concentration. n=3. (b) Alizarin red staining and quantitative analysis of ECM mineralization of MSCs after culturing for 21 days, scale bar=4 mm, n=3. (c) qRT-PCR analysis of the expression of osteoblast-specific genes for MSCs after culturing for 14 days normalized to *Gapdh* expression of cells on Ti on that day, n=3, and the columns in each group are Ti, Ti-AT₂, Ti-LA-AT₁, Ti-LA-AT₂ and Ti-LA-AT₄ Dunnett's multiple comparisons test. (d) qRT-PCR analysis of the expression of osteoblast-specific genes for MC3T3-E1 after culturing for 7 days and 14 days normalized to *β*-actin expression of cells on Ti on that day, n=3, Dunnett's multiple comparisons test. (e) Protein expression of *β*-catenin by Western blot measured from the MSCs cultured on the different samples for 14 days. (f) The quantitative analysis of *β*-catenin. (a-d, f) Data are presented as mean ± SD; *p < 0.05, **p < 0.01, ***p < 0.001; (a) two-way ANOVA with Dunnett's multiple comparisons test. (For interpretation of the references to color in this figure legend, the reader is referred to the web version of this article.)

performed to evaluate the expression of the extracellular matrix proteins OPN and OCN (stained in red fluorescence). Ti-LA-AT $_2$ has the best performance in any time points. Compared with Ti at 3 days, 7 days and 14 days, Ti-LA-AT $_1$, Ti-LA-AT $_2$, and Ti-LA-AT $_4$ have higher OCN protein expression levels after culturing for 3 days, 7 days and 14 days, which is consistent with the genetic expression levels shown in Fig. 6(c)–(d) and S14 and OPN shows a similar trend to that of OCN.

3.3. In vivo evaluation

In accordance with the different osteogenic ability of various samples *in vitro*, Ti, Ti-AT₂, Ti-LA-AT₁, Ti-LA-AT₂, and Ti-LA-AT₄ are selected for *in vivo* modeling to evaluate the bone formation activity. The Ti-based implants are implanted into the femurs of SD rat tibias (Fig. S17(a)–(c)). X-ray imaging (Fig. S17d) shows the implant position after 4 weeks *in vivo*. The new bone produced *in vivo* is analyzed by Micro-CT and histopathological evaluation after 4 weeks (Fig. 9(a) and (b)). Three different cylindrical areas approximately 2.0 mm in diameter and approximately 0.4 mm thick

around the implants as the interested section are calculated quantificationally to reduce error [48]. The object volume/tissue volume are assessed as a way of analyzing bone mass. The results of Ti, Ti-AT₂, Ti-LA-AT₁, Ti-LA-AT₂, and Ti-LA-AT₄ show increases of 29.024%, 29.844%, 31.996%, 42.113%, and 31.331%, respectively. Obviously, the Ti-LA-AT₂ has the largest bone mass (Fig. 9(b)).

To further evaluate the histopathological conditions around the implants after 4 weeks, Van Gieson's picro fuchsin staining and Safranin-O/Fast Green staining are performed (Fig. 9(c)-(f)). As indicated in Fig. 9(c), the red color represents mineralized bone tissue in the Van Gieson's picro fuchsin staining. Ti-LA-AT₂ performed better than Ti. The quantitative results showed that the Ti-LA-AT₂ group has great bone implant contact (83.866%) and bone area ratio (4.870%), far higher than the corresponding value for the pure Ti group (70.967% and 3.862%, respectively; Fig. 9(d) and (e)).

Safranin-O/Fast Green staining is used to assess osteogenic differentiation/cartilage differentiation. The green color represents osteogenesis, and the red or orange color represents cartilage. As shown in Fig. 9(f), the Ti-LA-AT₂ has many osteoblasts in the bone and no chondrocytes. The other groups have several chondrocytes.

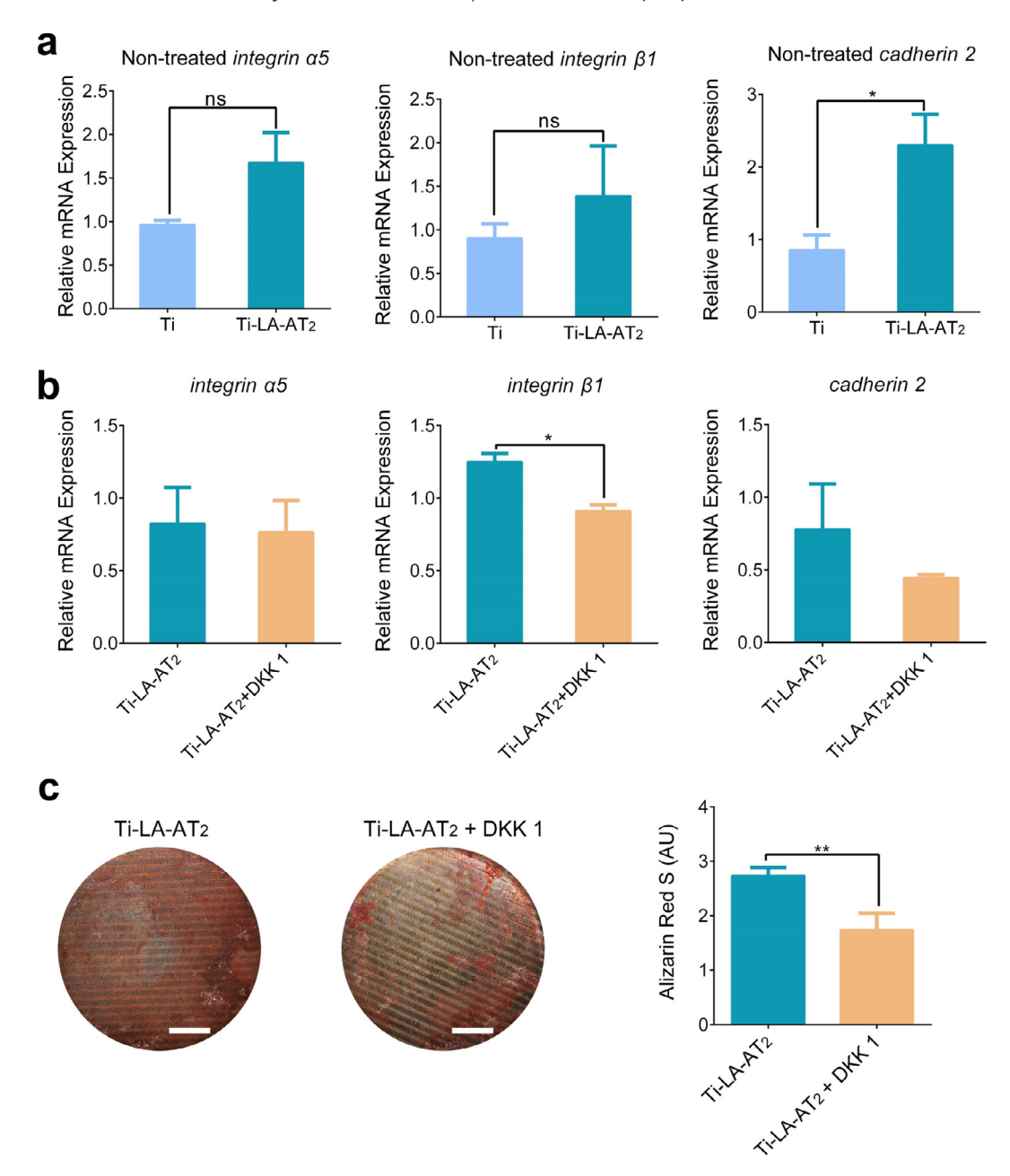


Fig. 7. (a) qRT-PCR analysis of the expression of genes for MSCs after culturing for 7 days normalized to *Gapdh* expression of cells on Ti and Ti-LA-AT₂, n = 3, t tests. (b) qRT-PCR analysis of the expression of genes for MSCs after culturing for 7 days normalized to *Gapdh* expression of cells on Ti-LA-AT₂ and Ti-LA-AT₂ +DKK1, n = 3, t tests. (c) Alizarin Red S staining of MSCs after culturing for 7 days on Ti-LA-AT₂ and Ti-LA-AT₂ +DKK1, n = 3, t tests, scale bar = 4 mm.

As shown in Fig. 9(g), the quantitative results indicate that Ti-LA-AT₂ has the best osteogenesis, approximately 65.4%, far higher than the ability of pure Ti (12.3%). Together, these findings reveal that ordered-micro and disordered-nano patterns can induce bone regeneration by regulating osteogenic factors *in vivo*. Immunohistochemical staining of iNOS and TGF β of different samples is used to assess inflammation around the implants, and iNOS represents that macrophages around the implant are differentiated into M1, while TGF β represents that macrophages around implant are differentiated into M2. The yellow color indicates positive expression. As shown in Fig. S18, Ti-LA-AT₁, Ti-LA-AT₂, and Ti-LA-AT₄ have little inflammation compared to Ti and Ti-AT₂.

4. Discussion

Ordered micro-waves and disordered nano-branches are obtained by laser and different concentration of KOH in hydrothermal

treatment. The process of KOH hydrothermal treatment is a general corrosion process involving the local cathode and anode regions. The hydrogen evolution reaction occurs in a cathode region, producing absorbed hydrogen in the near surface of the Ti plates. The absorbed hydrogen diffuses into the bulk of the Ti through the Gibbs energy gradient caused by a concentration gradient of absorbed hydrogen. A Ti surface that contains absorbed hydrogen dissolves more easily than untreated Ti. This process leads to the formation of a porous structure on Ti and Ti-based alloys [49]. While the laser-treated areas show large differences, the porous structure disappears, and a nanobranch-like structure emerges. There are two main factors influencing the formation of nanostructures on the Ti surface in an alkaline solution, i.e., a passive surface layer (Ti oxides and alkali titanate) and an H-containing layer. The passive layer tends to be more compact, thus forming a vital obstacle to cations and anions [50]. The laser-melted area has a more passive layer and less H, and the area treated by laser is harder

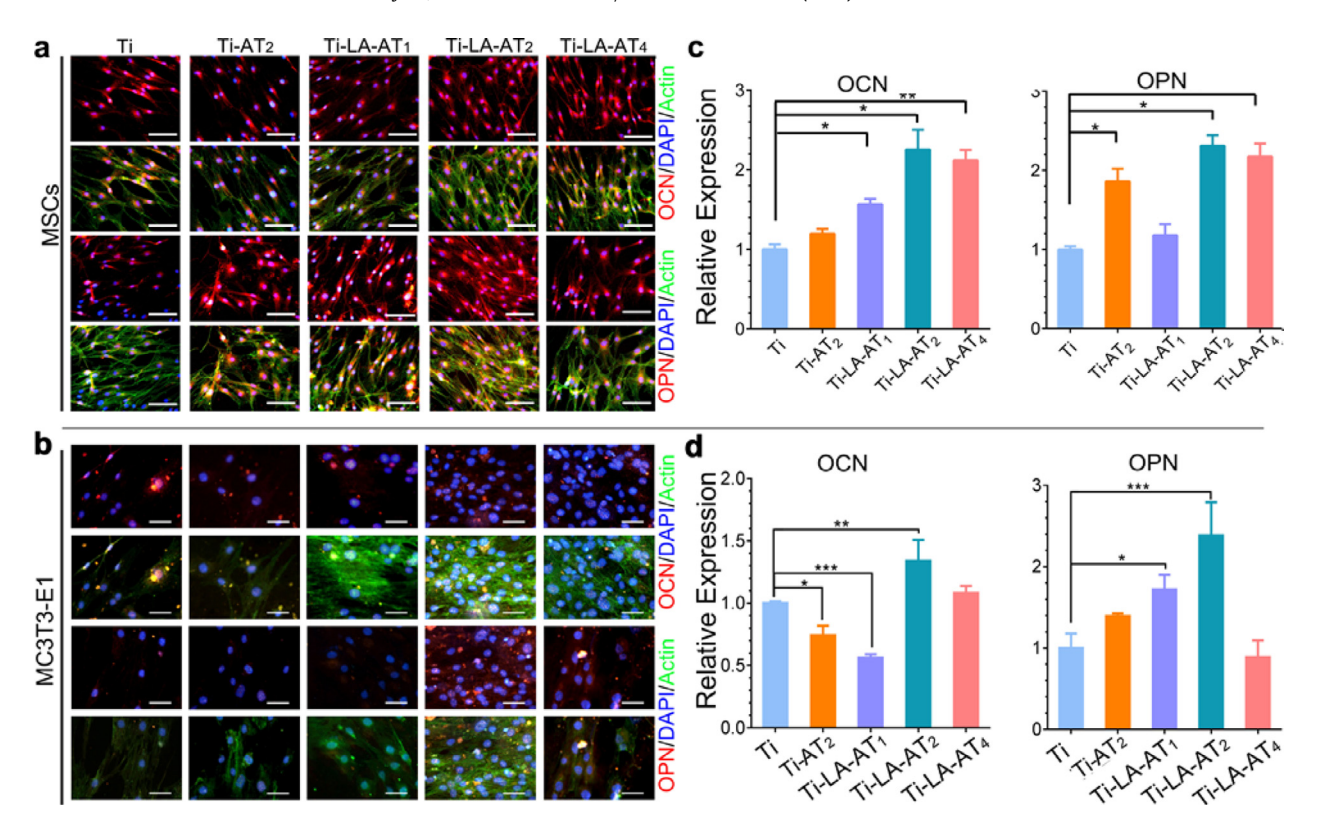


Fig. 8. Immunofluorescence staining of osteogenic markers: (a) OCN and OPN of MSCs on Ti, Ti-AT₂, Ti-LA-AT₁, Ti-LA-AT₂, and Ti-LA-AT₄ after culturing for 14 days (scale bars =100 μm). (b) OCN and OPN of MC3T3-E1 on Ti, Ti-AT₂, Ti-LA-AT₁, Ti-LA-AT₂, and Ti-LA-AT₄ after culturing for 14 days (scale bars =100 μm). (c) The MSCs quantitative analysis of OCN and OPN. n = 3. (d) The MC3T3-E1 quantitative analysis of OCN and OPN, and normalized to OPN or OCN expression of cells on Ti on that day, n = 3, t tests, n = 3. (c, d) Data are presented as mean \pm SD; *p < 0.05, **p < 0.01, ***p < 0.001; one-way analysis of variance (ANOVA) with Dunnett's multiple comparisons test.

to corrode than the untreated area. Therefore, a porous network forms on the ridges, whereas a discontinuous nanostructure appears from the laser-induced wave-like area. In addition, the pore size of the network structure is quite different for the three kinds of Ti plates, suggesting that the concentration of potassium hydroxide controls the nanostructure. The higher concentration of KOH leads to a denser distribution of the discontinuous branch-like nanostructures, as well as larger pore sizes in the network.

In general, the surface wettability could be divided into that on the flat surface and that on the uneven surface [39]. The former is rested with the surface free energy, based on the following equation [37]:

$$\gamma_{\rm sv} = \gamma_{\rm sl} + \gamma_{\rm lv} \cos \theta_{\rm Y} \tag{2}$$

where θ_Y is the contact angle, γ represents the surface free energy, and s, l, and v stand for solid state, liquid state, and gas state, respectively. The CAs of both Ti and Ti-AT₂ can be determined from Eq. (2). There are abundant hydrophilic hydroxyl groups after the alkali-heat process. The declining γ of Ti-AT₂ compared with the untreated Ti, and the CAs of Ti-AT₂ are less than that of Ti, thanks to the surface roughness. The detailed transformation of CAs and roughness is calculated by the following equation [39]:

$$\cos\theta_{\rm W} = {\rm rcos}\theta_{\rm Y} \tag{3}$$

where r is the surface roughness, $\theta_{\rm w}$ is the CAs in Eq. (3), and $\theta_{\rm Y}$ is the CAs in Eq. (2). $\theta_{\rm w}$ is the contact angle in the Wenzel model, and $\theta_{\rm Y}$ is the contact angle in Young's model. The CAs on Ti-LA-AT₁, Ti-LA-AT₂, and Ti-LA-AT₄ decreases slightly with the increasing concentration of KOH compared to Ti-AT₂, owing to the rough surface after the alkaline treatment [39].

To further analyze the influence of surface topography on MSC adhesion at an early stage, surface topography composed of ordered micro-waves and disordered nanobranches is designed. The

depth of the grooves and the height of ridges is several microns; contact guidance on ordered microtopography patterns affects cell alignment and creates anisotropy influence on cells [45]. A spacing of nanobranches is larger, the cells on the surface tend to have smaller focal adhesion and rounded cells due to the limited integrin units to form cluster and promote cell adhesion [51].

Microtopographies and nanotopographies have a contact guidance effect, which plays a vital role in regulating cell shape and influences biological activity [52]. Once exposed to serumcontaining medium, albumin, which is 100-1000 times higher than fibronectin and vitronectin towards content in medium, may absorb into the surface and form a protein layer before the cells adhere to the surface. Thereafter, ECM protein, including fibronectin and vitronectin, could replace albumin and likewise absorb into the surface, thereby modifying cell adhesion behavior on the surface [53]. Microtopographies and nanotopographies, together with increasing surface wettability, could enhance ECM protein adsorption including fibronectin, which could enhance cell adhesion and early bone healing [54]. Furthermore, the -OH group, which is created in hydrothermal treatment, also can accelerate cell adhesion on the surface. The cell adhesion, the early response of cells to the surface, would reflect different cell shapes and orientations, which can modify proliferation and differentiation [55]. Ordered microtopography could enhance the anisotropy of the cell nucleus, whereas disordered nanotopography could strengthen the isotropy of the cell nucleus [56]. Ti-LA-AT₂ is more anisotropic than the others. The interaction between the biomaterial and the cell influences cell fate [57]. A recent study demonstrated that a change in nuclear shape would lead to chromatin condensation [58]. Deformation in the nucleus would change the behavior and fate of cells.

Meanwhile, selective laser melting brings ordered microtopography to Ti, and the cells on samples can show more anisotropy. After the Ti is treated with the alkali solution, the disordered nan-

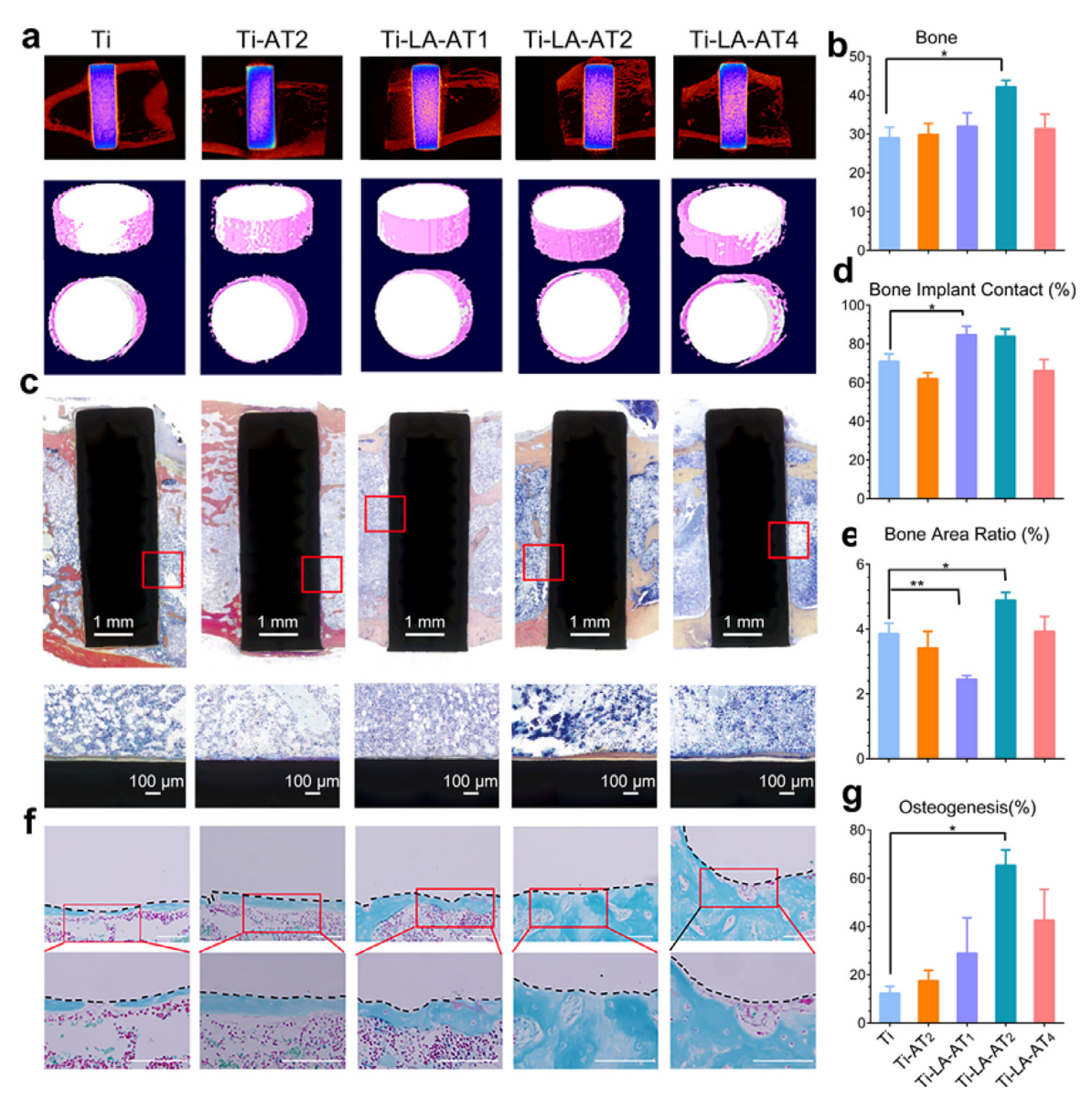


Fig. 9. Evaluation of *in vivo* bone formation after 4 weeks. (a) Micro-CT 2D and 3D images of new bone formation around the Ti, Ti-AT₂, Ti-LA-AT₁, Ti-LA-AT₂, and Ti-LA-AT₄ implants. (b) The amount of new bone generated is quantitated by measurement of Micro-CT 3D images of bone remodeling, n = 6. (c-g) Histological characteristics and histomorphometric evaluation at the bone—implant interfaces: (c) Van Gieson's picro fuchsin staining- (scale bars = 100 and 200 μ m). The nucleus of the osteoblast is stained blue and the new bone is stained red. (d) Histomorphometric measurements of new bone area rate. The area is 250 μ m around the implant. (e) The histomorphometric measurements of bone—implant contact. (f) Safranin-O/Fast Green staining. The green color is osteogenesis, and the red or orange color is cartilage (scale bars = 100 μ m). (g) Histomorphometric measurements of osteogenesis. (b, d, e, g) The columns in each group are Ti, Ti-AA-T₁, Ti-LA-AT₂ and Ti-LA-AT₄, and data are presented as mean \pm SD; *p < 0.05, **p < 0.01, **p < 0.001, **p < 0.01, **p < 0.001; One-way analysis of variance (ANOVA) with Dunnett's multiple comparisons test. (For interpretation of the references to color in this figure legend, the reader is referred to the web version of this article.)

otopography appears. This structure will weaken the anisotropy. The spacing between the nanobranch is too long, and the Ti-LA-AT₂ has a more obvious orientation than Ti-LA-AT₁. The cell nuclei on Ti-LA-AT₄ tend to show isotropy, mainly because of the 4 M KOH solution. Cell spreading and orientation are strongly correlated to phenotype [39]. Osteoblasts present orientation behaviors and have a high level of cytoskeletal tension. The formation of pseudopodia is related to the spacing of nanotopography [59]. The ordered micro-waves have a vital influence on the cell shape [60]. Combining anisotropy induced by ordered micro-waves and isotropic poverty created by disordered nanobranches creates appropriate anisotropy and is beneficial for osteogenic differentiation [61].

Microtopography reduces cell proliferation, compared with an unmodified Ti surface. Meanwhile, nanotopography added to microtopography could enhance cell proliferation, which is compared to microtopography and the unmodified Ti surface. Furthermore, surface wettability also benefits cell proliferation. High cell proliferation may produce greater bone mass in *vivo* and further benefit bone-implant binding [46].

That MSCs and MC3T3-E1 differentiate into osteoblasts is vital to implant osseointegration [62]. Microtopography added to nanotopography can assist MSCs and MC3T3-E1 to differentiate into osteoblast [63]. However, the overlaid isotropic and anisotropic cues are poorly understood in the field. The mRNA expression of *Runx2*, *Alp*, *Ocn*, and *Opn* of Ti-LA-AT₂ is higher than Ti at any point in time. Immunofluorescence staining of OPN and OCN, mineralization assay, and Western blot yield has similar results.

When cells are put on the patterned surface, integrin α_5 and integrin β_1 on the cell membrane can sense the cues. DSH bind-

ing with FZD results in nonphosphorylated β -catenin to enter into cytoplasm. This quantity of β -catenin is increased in the cytoplasm which is positively relative to osteoblast differentiation. Large quantities of β -catenin are found in the cytoplasm, and more β -catenin is translated into the nuclei, where it interacts with Tef/Lef to activate the expression of phenotypic osteoblast genes [64]. To further verify whether Wnt/ β -catenin signaling gets involved in osteogenic differentiation on the Ti surface, DKK1 is used to block the canonical Wnt signaling pathway. The results show that DKK1 not only inhibits the expression of Wnt/ β -catenin signaling genes ($integrin\alpha 5$, $integrin\beta 1$, and cadherin 2) but also that Wnt/ β -catenin signaling is related with the osteogenic differentiation caused by overlaid isotropic and anisotropic cues.

5. Conclusions

In summary, the desired anisotropy and isotropy can modulate cell migration through osteoblast differentiation and enhance osseointegration between the bone and implant. In this work, the ordered-micro and disordered-nano patterned structures could form overlaid isotropic and anisotropic cues and induce nuclear orientation by triggering signaling events involving Wnt/ β -catenin signaling, overcoming the limitation that cells can only sense cues over a limited distance by relaying cues through nano/micro topography. That canonical Wnt signaling inhibitor dickkopf1 (Dkk1) is further used to demonstrate osteogenic differentiation induced by ordered-micro and disordered-nano patterned structures, which is related with Wnt/ β -catenin signaling. Meanwhile, we put forward the means of designing surface topography and analyzing interaction models between cells and materials in vitro and predict effective bone regeneration in vivo. Furthermore, by combining our outcomes and understanding with regard to osseointegration, we have the potential to find new surface structure and highly efficient bone formation materials.

Data availability

The authors confirm that the raw/processed data supporting the findings of this study are available from the corresponding author upon reasonable request.

Declaration of Competing Interest

All the authors declare that there are no conflicts of interest.

CRediT authorship contribution statement

Jieni Fu: Conceptualization, Investigation, Methodology, Data curation, Formal analysis, Writing - original draft, Writing - review & editing, Validation. Xiangmei Liu: Conceptualization, Supervision, Data curation, Formal analysis, Validation. Lei Tan: Writing - review & editing, Validation. Zhenduo Cui: Writing - review & editing, Validation. Yanqin Liang: Writing - review & editing, Validation. Shengli Zhu: Writing - review & editing, Validation. Yufeng Zheng: Writing - review & editing, Validation. Kelvin Wai Kwok Yeung: Writing - review & editing, Validation. Paul K Chu: Writing - review & editing, Validation, Conceptualization, Writing - review & editing.

Acknowledgments

This work is supported by the National Key R&D Program of China No. 2016YFC1100600 (sub-project 2016YFC1100604), National Natural Science Foundation of China, Nos. 51671081, 51871162, and 51801056, Natural Science Fund of Hubei Province,

2018CFA064, and Hong Kong ITC (ITS/287/17, GHX/002/14SZ), Health and Medical Research Fund (03142446), as well as Hong Kong RGC GRF (17214516) and RGC/NSFC (N_HKU725-16).

Supplementary materials

Supplementary material associated with this article can be found, in the online version, at doi:10.1016/j.actbio.2019.10.041.

References

- E.D. Tabdanov, V.V. Puram, Z. Win, A. Alamgir, P.W. Alford, P.P. Provenzano, Bimodal sensing of guidance cues in mechanically distinct microenvironments, Nat. Commun. 9 (2018) 4891, doi:10.1038/s41467-018-07290-y.
- [2] M.K. Driscoll, C. McCann, R. Kopace, T. Homan, J.T. Fourkas, C. Parent, W. Losert, Cell shape dynamics: from waves to migration, PLoS Comput. Biol. 8 (2012) e1002392, doi:10.1371/journal.pcbi.1002392.
- [3] L. Tan, J. Li, X. Liu, Z. Cui, X. Yang, S. Zhu, Z. Li, X. Yuan, Y. Zheng, K.W.K. Yeung, H. Pan, X. Wang, S. Wu, Rapid biofilm eradication on bone implants using red phosphorus and near-infrared light, Adv Mater 30 (2018) e1801808, doi:10.1002/adma.201801808.
- [4] Y. Li, X. Liu, L. Tan, Z. Cui, X. Yang, Y. Zheng, K.W.K. Yeung, P.K. Chu, S. Wu, Rapid sterilization and accelerated wound healing using Zn2+ and graphene oxide modified g-C3N4 under dual light irradiation, Adv. Funct. Mater. 28 (2018) 1800299, doi:10.1002/adfm.201800299.
- [5] S. Oh, K.S. Brammer, Y.S.J. Li, D. Teng, A.J. Engler, S. Chien, S. Jin, Stem cell fate dictated solely by altered nanotube dimension, Proc. Natl. Acad. Sci. USA. 106 (2008) 2130–2135, doi:10.1073/pnas.0813200106.
- [6] R. McBeath, D.M. Pirone, C.M. Nelson, K. Bhadriraju, C.S. Chen, Cell shape, cytoskeletal tension, and Rhoa regulate stem cell lineage commitment, Dev. Cell 6 (2004) 483–495.
- [7] K.A. Kilian, B. Bugarija, B.T. Lahn, M. Mrksich, Geometric cues for directing the differentiation of mesenchymal stem cells, Proc. Natl. Acad. Sci. USA 107 (2010) 4872–4877, doi:10.1073/pnas.0903269107.
- [8] N. Andrew, R.H. Insall, Chemotaxis in shallow gradients is mediated independently of Ptdins 3-kinase by biased choices between random protrusions, Nat. Cell Biol. 9 (2007) 193–200, doi:10.1016/S1534-5807(04)00075-9.
- [9] R.P. Xiang Yao, J. Ding, Cell-material interactions revealed via material techniques of surface patterning, Adv. Mater. (2013), doi:10.1002/adma.201301762.
- [10] C.J. Bettinger, R. Langer, J.T. Borenstein, Engineering substrate topography at the micro-and nanoscale to control cell function, Angew. Chem. Int. Ed. Engl. 48 (2009) 5406–5415, doi:10.1002/anie.200805179.
- [11] C.A. Parent, P.N. Devreotes, A cell's sense of direction, Science 284 (1999) 765–769, doi:10.1126/science.284.5415.765.
- [12] A. Shellard, A. Szabó, X. Trepat, R. Mayor, Supracellular contraction at the rear of neural crest cell groups drives collective chemotaxis, Science 362 (2018) 339–343, doi:10.1126/science.aau3301.
- [13] A. Elbaz, J. Lu, B. Gao, F. Zheng, Z. Mu, Y. Zhao, Z. Gu, Chitin-based anisotropic nanostructures of butterfly wings for regulating cells orientation, Polymers (Basel) 9 (2017), doi:10.3390/polym9090386.
- [14] M.K. Driscoll, X. Sun, C. Guven, J.T. Fourkas, W. Losert, Cellular contact guidance through dynamic sensing of nanotopography, Nano Lett 8 (2015) 3546– 3555, doi:10.1021/nn406637c.
- [15] B. W6jciak-Stothard, Z. Madeja, W. Korohoda, A. Curtls, C. Wilkinson, Activation of macrophage-like cells by multiple grooved substrata. Topographical control of cell behaviour, Cell Bio. Int. 19 (1995) 485–490, doi:10.1006/cbir.1995.1092.
- [16] A. Wennerberg, T. Albrektsson, Effects of titanium surface topography on bone integration: a systematic review, Clin. Oral Implan. Res. 20 (2009) 172–184, doi:10.1111/j.1600-0501.
- [17] N. Huebsch, E. Lippens, K. Lee, M. Mehta, S.T. Koshy, M.C. Darnell, R.M. Desai, C.M. Madl, M. Xu, X. Zhao, O. Chaudhuri, C. Verbeke, W.S. Kim, K. Alim, A. Mammoto, D.E. Ingber, G.N. Duda, D.J. Mooney, Matrix elasticity of void-forming hydrogels controls transplanted-stem-cell-mediated bone formation, Nat. Mater. 14 (2015) 1269–1277, doi:10.1038/nmat4407.
- [18] L. Meirelles, A. Arvidsson, T. Albrektsson, A. Wennerberg, Increased bone formation to unstable nano rough titanium implants, Clin. Oral Implants Res. 18 (2007) 326–332, doi:10.1111/j.1600-0501.2006.01308.x.
- [19] N. Jiang, Z. Guo, D. Sun, Y. Li, Y. Yang, C. Chen, L. Zhang, S. Zhu, Promoting osseointegration of Ti implants through micro/nanoscaled hierarchical ti phosphate/ti oxide hybrid coating, ACS Nano 12 (2018) 7883–7891, doi:10.1021/ acsnano.8b02227.
- [20] D. Nepal, M.S. Onses, K. Park, M. Jespersen, C.J. Thode, P.F. Nealey, R.A. Vaia, Control over position, orientation, and spacing of arrays of gold nanorods using chemically nanopatterned surfaces and tailored particle particle surface interactions. ACS Nano 6 (2012) 5693–5701. doi:10.1021/nn301824u.
- [21] M. Peer, M. Lusardi, K.F. Jensen, Facile soft-templated synthesis of high-surface area and highly porous carbon nitrides, Chem. Mater. 29 (2017) 1496–1506, doi:10.1021/acs.chemmater.6b03570.
- [22] C. Tang, E.M. Lennon, G.H. Fredrickson, E.J. Kramer, C.J. Hawker, Evolution of block copolymer lithography to highly ordered square arrays, Science 322 (2008) 429–432, doi:10.1126/science.1162950.
- [23] İ. Milinkovic, R. Rudolf, K.T. Raic, Z. Aleksic, V. Lazic, A. Todorovic, D. Stamenkovic, aspects of titanium-implant surface modification at the micro and nano levels, Mater. Tehnol. 46 (2012) 251–256.

- [24] A. Ray, O. Lee, Z. Win, R.M. Edwards, P.W. Alford, D.H. Kim, P.P. Provenzano, Anisotropic forces from spatially constrained focal adhesions mediate contact guidance directed cell migration, Nat. Commun. 8 (2017) 14923, doi:10.1038/ ncomms14923.
- [25] H. Ananth, V. Kundapur, H.S. Mohammed, M. Anand, G.S. Amarnath, S. Mankar, A review on biomaterials in dental implantology, Int. J. Biomed. Sci. 11 (2015) 113–120.
- [26] T. Razafiarison, C.N. Holenstein, T. Stauber, M. Jovic, E. Vertudes, M. Loparic, M. Kawecki, L. Bernard, U. Silvan, J.G. Snedeker, Biomaterial surface energy-driven ligand assembly strongly regulates stem cell mechanosensitivity and fate on very soft substrates, Proc. Natl. Acad. Sci. USA 115 (2018) 4631–4636, doi:10.1073/pnas.1704543115.
- [27] F. Chowdhury, S. Na, D. Li, Y.C. Poh, T.S. Tanaka, F. Wang, N. Wang, Material properties of the cell dictate stress-induced spreading and differentiation in embryonic stem cells, Nat. Mater. 9 (2010) 82–88.
- [28] M.J. Dalby, N. Gadegaard, R. Tare, A. Andar, M.O. Riehle, P. Herzyk, C.D. Wilkinson, R.O. Oreffo, The control of human mesenchymal cell differentiation using nanoscale symmetry and disorder, Nat. Mater. 6 (2007) 997–1003, doi:10.1038/nmat2563.
- [29] S. Karimi, T. Nickchi, A. Alfantazi, Effects of bovine serum albumin on the corrosion behaviour of AlSI 316L, Co-28Cr-6Mo, and Ti-6Al-4V alloys in phosphate buffered saline solutions, Corros. Sci. 53 (2011) 3262-3272, doi:10.1016/j.corsci.2011.06.009.
- [30] J. Ryu, S.H. Ku, H. Lee, C.B. Park, Mussel-Inspired polydopamine coating as a universal route to hydroxyapatite crystallization, Adv.Funct. Mater. 20 (2010) 2132–2139, doi:10.1002/adfm.200902347.
- [31] Q. Jia, D. Gu, Selective laser melting additive manufacturing of inconel 718 superalloy parts: densification, microstructure and properties, J. Alloys Comp. 585 (2014) 713–721, doi:10.1016/j.jallcom.2013.09.171.
- [32] C. Zhang, J. Zhou, H. Shen, Role of capillary and thermocapillary forces in laser polishing of metals, J. Manuf. Sci. Eng. Trans. ASME 139 (2017), doi:10.1115/1. 4035468.
- [33] K. Cai, M. Lai, W. Yang, R. Hu, R. Xin, Q. Liu, K.L. Sung, Surface engineering of titanium with potassium hydroxide and its effects on the growth behavior of mesenchymal stem cells, Acta Biomater. 6 (2010) 2314–2321, doi:10.1016/j. actbio.2009.11.034.
- [34] G. Liu, J. Zou, Q. Tang, X. Yang, Y. Zhang, Q. Zhang, W. Huang, P. Chen, J. Shao, X. Dong, Surface modified Ti3C2 MXene nanosheets for tumor targeting photothermal/photodynamic/chemo synergistic therapy, ACS Appl. Mater. Interfaces 9 (2017) 40077–40086, doi:10.1021/acsami.7b13421.
- [35] C. Kim, M.R. Kendall, M.A. Miller, C.L. Long, P.R. Larson, M.B. Humphrey, A.S. Madden, A.C. Tas, Comparison of titanium soaked in 5 M NaOH or 5M KOH solutions, Mater. Sci. Eng. C 33 (2013) 327–339, doi:10.1016/j.msec.2012.08.047.
- [36] G. Yang, L. Wang, S. Peng, J. Wang, D. Ji, W. Yan, S. Ramakrishna, In situ fabrication of hierarchically branched TiO₂ nanostructures: enhanced performance in photocatalytic H2 evolution and Li-ion batteries, Small (2017), doi:10.1002/smll.201702357.
- [37] X. Liu, H.C. Man, Laser fabrication of ag-ha nanocomposites on Ti6Al4V implant for enhancing bioactivity and antibacterial capability, Mater. Sci. Eng. C 70 (2017) 1–8, doi:10.1016/j.msec.2016.08.059.
- [38] M. He, X. Chen, K. Cheng, W. Weng, H. Wang, Enhanced osteogenic activity of TiO₂ nanorod films with microscaled distribution of Zn-cap, ACS Appl. Mater. Interfaces 8 (2016) 6944–6952, doi:10.1021/acsami.6b01284.
- [39] Y. Zhang, X. Liu, Z. Li, S. Zhu, X. Yuan, Z. Cui, X. Yang, P.K. Chu, S. Wu, Nano Ag/ZnO-incorporated hydroxyapatite composite coatings: highly effective infection prevention and excellent osteointegration, ACS Appl. Mater. Interfaces 10 (2017) 1266–1277, doi:10.1021/acsami.7b17351.
- [40] X. Wang, Y. Li, J. Xiong, P.D. Hodgson, C. Wen, Porous TiNbZr alloy scaffolds for biomedical applications, Acta Biomater. 5 (2009) 3616–3624, doi:10.1016/j. actbio.2009.06.002.
- [41] S. Wu, Z. Weng, X. Liu, K.W.K. Yeung, P.K. Chu, Functionalized TiO₂ based nanomaterials for biomedical applications, Adv. Funct. Mater. 24 (2014) 5464–5481, doi:10.1002/adfm.201400706.
- [42] W. Zhao, J. Lemaitre, P. Bowen, A comparative study of simulated body fluids in the presence of proteins, Acta Biomater. 53 (2017) 506–514, doi:10.1016/j. actbio.2017.02.006.
- [43] T.C. von Erlach, S. Bertazzo, M.A. Wozniak, C.M. Horejs, S.A. Maynard, S. Attwood, B.K. Robinson, H. Autefage, C. Kallepitis, A. Del Rio Hernandez, C.S. Chen, S. Goldoni, M.M. Stevens, Cell-geometry-dependent changes in plasma membrane order direct stem cell signalling and fate, Nat. Mater. 17 (2018) 237–242, doi:10.1038/s41563-017-0014-0.
- [44] L. Yang, Z. Gong, Y. Lin, V. Chinthapenta, Q. Li, T.J. Webster, B.W. Sheldon, Disordered topography mediates filopodial extension and morphology of cells on stiff materials, Adv. Funct. Mater. 27 (2017) 1702689, doi:10.1002/adfm. 201702689.

- [45] C.S. Kim, J.H. Kim, B. Kim, Y.S. Park, H.K. Kim, H.T. Tran, S.H. Kim, H. Jeon, S. Kim, J.H. Sim, H.M. Shin, G. Kim, Y.J. Baik, K.-J. Lee, H.-Y. Kim, T.J. Yun, Y.S. Kim, H.-R. Kim, A specific groove pattern can effectively induce osteoblast differentiation, Adv. Funct. Mater. 27 (2017) 1703569, doi:10.1002/adfm.201703569.
- [46] P. Jiang, J. Liang, R. Song, Y. Zhang, L. Ren, L. Zhang, P. Tang, C. Lin, Effect of octacalcium-phosphate-modified micro/nanostructured titania surfaces on osteoblast response, ACS Appl. Mater. Interfaces 7 (2015) 14384–14396, doi:10.1021/acsami.5b03172.
- [47] R. Baron, M. Kneissel, WNT signaling in bone homeostasis and disease: from human mutations to treatments, Nat. Med. 19 (2013) 179–192, doi:10.1038/nm. 3074.
- [48] D. Fleischmann, F.E. Boas, CT artifacts: causes and reduction techniques, Imaging Med. 4 (2012) 1755–5191.
- [49] S. Tanaka, H. Tobimatsu, Y. Maruyama, T. Tanaki, G. Jerkiewicz, Preparation and characterization of microporous layers on titanium, ACS Appl. Mater. Interfaces 1 (2009) 2312–2319, doi:10.1021/am900474h.
- [50] S. Tanaka, Y. Fukushima, I. Nakamura, T. Tanaki, G. Jerkiewicz, Preparation and characterization of microporous layers on titanium by anodization in sulfuric acid with and without hydrogen charging, ACS Appl. Mater. Interfaces 5 (2013) 3340–3347, doi:10.1021/am900474h.
- [51] M.J. Dalby, N. Gadegaard, R.O. Oreffo, Harnessing nanotopography and integrin-matrix interactions to influence stem cell fate, Nat. Mater. 13 (2014) 558–569.
- [52] Y. Li, Y. Xiao, C. Liu, The horizon of materiobiology: a perspective on material-guided cell behaviors and tissue engineering, Chem. Rev. 117 (2017) 4376–4421, doi:10.1021/acs.chemrev.6b00654.
- [53] Y. Arima, H. Iwata, Effect of wettability and surface functional groups on protein adsorption and cell adhesion using well-defined mixed self-assembled monolayers, Biomaterials 28 (2007) 3074–3082, doi:10.1016/j.biomaterials. 2007.03.013.
- [54] J.W. Park, Y.J. Kim, C.H. Park, D.H. Lee, Y.G. Ko, J.H. Jang, C.S. Lee, Enhanced osteoblast response to an equal channel angular pressing-processed pure titanium substrate with microrough surface topography, Acta Biomater 5 (2009) 3272–3280, doi:10.1016/j.actbio.2009.04.038.
- [55] N.J. Hallab, K.J. Bundy, K. O'Connor, R. Clark, R.L. Moses, Cell adhesion to biomaterials: correlations between surface charge, surface roughness, adsorbed protein, and cell morphology, j, Long-Term Eff. Med. Implants 5 (1995) 209–231.
- [56] D. Caballero, L. Palacios, P.P. Freitas, J. Samitier, An interplay between matrix anisotropy and actomyosin contractility regulates 3D-Directed cell migration, Adv. Funct. Mater. 27 (2017) 1702322, doi:10.1002/adfm.201702322.
- [57] C. Cha, W.B. Liechty, A. Khademhosseini, N.A. Peppas, Designing biomaterials to direct stem cell fate, ACS Nano 6 (2012) 9353–9358, doi:10.1021/nn304773b.
- [58] T. Heydari, M. Heidari, O. Mashinchian, M. Wojcik, K. Xu, M.J. Dalby, M. Mahmoudi, M.R. Ejtehadi, Development of a virtual cell model to predict cell response to substrate topography, ACS Nano 11 (2017) 9084–9092, doi:10.1021/acsnano.7b03732.
- [59] R. Oria, T. Wiegand, J. Escribano, A. Elosegui-Artola, J.J. Uriarte, C. Moreno-Pulido, I. Platzman, P. Delcanale, L. Albertazzi, D. Navajas, X. Trepat, J.M. Garcia-Aznar, E.A. Cavalcanti-Adam, P. Roca-Cusachs, Force loading explains spatial sensing of ligands by cells, Nature 552 (7684) (2017) 219–224.
- [60] T.L. Downing, J. Soto, C. Morez, T. Houssin, A. Fritz, F. Yuan, J. Chu, S. Patel, D.V. Schaffer, S. Li, Biophysical regulation of epigenetic state and cell reprogramming, Nat. Mater. 12 (12) (2013) 1154–1162.
- [61] Q. Xing, Z. Qian, B. Kannan, M. Tahtinen, F. Zhao, Osteogenic differentiation evaluation of an engineered extracellular matrix based tissue sheet for potential periosteum replacement, ACS Appl. Mater. Interfaces 7 (41) (2015) 23239–23247.
- [62] D. Hu, K. Li, Y. Xie, H. Pan, J. Zhao, L. Huang, X. Zheng, The combined effects of nanotopography and Sr ion for enhanced osteogenic activity of bone marrow mesenchymal stem cells (BMSCs), J. Biomater. Appl. 31 (8) (2017) 1135– 1147
- [63] L. Lin, H. Wang, M. Ni, Y. Rui, T.-Y. Cheng, C.-K. Cheng, X. Pan, G. Li, C. Lin, Enhanced osteointegration of medical titanium implant with surface modifications in micro/nanoscale structures, J. Orthop. Transl. 2 (1) (2014) 35–42.
- [64] L. Mao, J. Liu, J. Zhao, J. Chang, L. Xia, L. Jiang, X. Wang, K. Lin, B. Fang, Effect of micro-nano-hybrid structured hydroxyapatite bioceramics on osteogenic and cementogenic differentiation of human periodontal ligament stem cell via WNT signaling pathway, Int. J. Nanomed. 10 (2015) 7031–7044.